Monthly Notices
of the
ROYAL ASTRONOMICAL SOCIETY

MNRAS **452,** 173–192 (2015) doi:10.1093/mnras/stv1309

A kinematically unbiased search for nearby young stars in the Northern hemisphere selected using SuperWASP rotation periods

A. S. Binks,★ R. D. Jeffries★ and P. F. L. Maxted★

Astrophysics Group, School of Chemistry and Physics, Keele University, Keele, Staffordshire ST5 5BG, UK

Accepted 2015 June 8. Received 2015 June 1; in original form 2015 April 27

ABSTRACT

We present a kinematically-unbiased search to identify young, nearby low-mass members of kinematic moving groups (MGs). Objects with both rotation periods shorter than 5 d in the SuperWASP All-Sky Survey and X-ray counterparts in the *ROSAT* All-Sky Survey were chosen to create a catalogue of several thousand rapidly rotating, X-ray active FGK stars. These objects are expected to be either young single stars or tidally locked spectroscopic binaries. We obtained optical spectra for a sub-sample of 146 stars to determine their ages and kinematics, and in some cases repeat radial velocity measurements were used to identify binarity. 26 stars are found to have lithium abundances consistent with an age of $\leq$200 Myr, and show no evidence for binarity and in most cases measurements of H α and $v \sin i$ support their youthful status. Based on their youth, their radial velocities and estimates of their three-dimensional kinematics, we find 11 objects that may be members of known MGs, eight that do not appear associated with any young MG and a further seven that are close to the kinematics of the recently proposed 'Octans-Near' MG, and which may be the first members of this MG found in the Northern hemisphere. The initial search mechanism was ∼18 per cent efficient at identifying likely-single stars younger than 200 Myr, of which 80 per cent were early-K spectral types.

Key words: stars: late-type – stars: pre-main-sequence.

1 INTRODUCTION

In a series of publications in the 1960s, Olin Eggen hypothesized the existence of a 'Local Association' of comoving, early-type stars in the solar vicinity (Eggen 1961, 1965). This association (also known as the Pleiades moving group) included members of the Pleiades, α Persei and IC 2602 open clusters, and roughly one-third of the B7-A0 stars within 300pc (Eggen 1983).

Following Eggen's hypothesis, detailed observations of several young, chromospherically active, fast-rotating, late-type stars led to the suggestion that they too were part of the Local Association (e.g. AB Dor, PZ Tel, Innis, Coates & Thompson 1988; BO Mic, Anders et al. 1993; LO Peg, Jeffries et al. 1994). Follow-up spectroscopy of optical counterparts to coronally active late-type stars found in EUV and X-ray surveys found that a large fraction were comoving with the Local Association (Jeffries & Jewell 1993); many were as young or younger than the Pleiades (∼100 Myr) as evidenced by the presence of lithium in their photospheres, which is otherwise burned rapidly during the pre-main sequence (PMS) in low-mass stars (Jeffries 1995). Subsequent work (e.g. Zuckerman & Webb 2000; Torres et al. 2000; Montes et al. 2001; Zuckerman et al. 2001; Zuckerman & Song 2004) suggested that the Local Association has kinematic and spatial substructure, consisting of several different coeval, comoving streams of stars at a range of young ages, that have been collectively termed 'nearby young moving groups' (hereafter referred to as MGs; Zuckerman & Song 2004; Torres et al. 2008). The origin of these MGs is still an open question. They may be the result of the dissolution of young open clusters, with members of each MG sharing a common birthplace as well as common kinematics. For instance, De Silva et al. (2013) found that stars in the Argus MG and the IC 2391 open cluster shared common chemical abundances and kinematics. However, an abundance analysis of a population of objects in the AB Doradus MG (ABDMG) by Barenfeld et al. (2013) indicates that approximately half of the previously suggested members do *not* share a similar chemical composition, arguing against a common origin.

Finding young stars in the solar neighbourhood is important because they represent some of the best observational targets for understanding the early evolution of stars and their surrounding circumstellar environments and planetary systems (e.g. Dent et al. 2013; Brandt et al. 2014; Bowler et al. 2015). They are much closer than their equivalents in young clusters and star forming regions, offering advantages both in terms of sensitivity and spatial resolution. If stars can be linked to particular coeval MGs, then their ages can reasonably be assumed similar to that MG as a whole. At ages of 10–100 Myr gas giant planets around MG members are expected

★E-mail: a.s.binks@keele.ac.uk (ASB); r.d.jeffries@keele.ac.uk (RDJ); p.maxted@keele.ac.uk (PFLM)

to be much more luminous than in older systems, and young stars are frequently surrounded by debris discs that may evidence the formation of terrestrial planets or provide diagnostic indicators of unseen planets. Lower mass MG members potentially provide even better targets to investigate planets and circumstellar environments because their lower luminosities enhance the contrast with giant planets of a given mass. Examples of work that exploits the youth and proximity of MG members includes the high contrast infrared imaging detection of multiple planets surrounding the 30 Myr old A-type dwarf, HR 8799, a member of the Columba MG (Marois et al. 2008, 2010), and the identification of a planet around the A6V star β Pic; the eponymous member of the β Pictoris MG (BPMG; Lagrange et al. 2010).

Much work has focused on finding new low-mass MG members using both kinematic selection and kinematically unbiased surveys. Kinematic selection may be efficient at discovering new members of known MGs, but precludes the discovery of nearby, young objects that are not members of these groups. Examples include the proper-motion-selected searches reported by Schlieder, Lépine & Simon (2010, 2012) or the work of Malo et al. (2013, 2014a) and Gagné et al. (2014, 2015), who used both positions and Galactic velocities to assign probabilities of membership to new candidate members of several known MGs.

Kinematically unbiased searches are possible but less efficient. For example, from an initial sample of 405 late-type stars within 25 pc of the Sun, Maldonado et al. (2010) found only 6 per cent that may be candidate members of known MGs based on their space motions. A more focused approach is to pre-select stars which are likely to be young based on their magnetic activity. Young stars are magnetically active as a result of their fast rotation, convective envelopes and consequent dynamo-generated magnetic fields; this activity is manifested as chromospheric and coronal emission that can be detected via optical emission lines or UV and X-ray flux. Examples of this approach can be found in the earlier works of Jeffries (1995) and Montes et al. (2001), but more recently Torres et al. (2006), Lépine & Simon (2009), da Silva et al. (2009) and Shkolnik et al. (2011). Notably, Shkolnik et al. (2012) pre-selected a sample of nearby, X-ray active M-dwarfs, finding many new MG members but also finding that about 50 per cent of the young M-dwarfs could not be assigned to any of the currently known MGs.

Here we describe a new, kinematically unbiased method to select young stars that relies on the fact that stellar rotation is strongly age dependent. At young ages, a large fraction of low-mass stars have fast rotation rates (rotation periods less than a few days – e.g. Patten & Simon 1996; Krishnamurthi et al. 1998). Angular momentum loss due to magnetized stellar winds leads to spin-down on a mass-dependent time-scale, ranging from $\simeq$50 Myr for G-stars to hundreds of Myr for M-dwarfs (see for example Barnes 2003). Messina et al. (2010) report rotation periods of the order of several days or less for many MG members, confirming that a selection based on a short rotation period is likely to favour young stars, although may be contaminated by members of older, tidally-locked short period binary systems. Confirming the youth of candidates requires high-resolution spectroscopy. Young F-,G- and K-stars should have large abundances of lithium in their photospheres (e.g. Sestito & Randich 2005; Jeffries 2006) and multiple radial velocity (RV) measurements can be used to identify short-period binary systems.

In this paper, we report our initial efforts to find young, nearby stars using a parent sample of fast-rotating, active stars selected from the union of the SuperWASP transiting planet survey and the *ROSAT* X-ray all-sky survey. These candidates were followed up with high-resolution spectroscopy at the Nordic Optical Telescope (NOT) and Isaac Newton Telescope (INT). In Section 2, we describe how rotation periods were estimated from the SuperWASP photometry data base. The initial candidate selection is described in Section 3 along with details of the spectroscopic observations. In Section 4, we describe the techniques used to measure radial and rotational velocities, temperatures, chromospheric activity and Li abundances. The multiple methods that were used to constrain the ages of the observed targets are discussed in Section 5, and in Section 6 the space motions of the young, Li-rich targets are calculated and compared to known MGs. We provide a discussion of individual objects in Section 7 and in Section 8 we discuss the potential of a repeat survey, focusing on the efficiency and relative success of this work at identifying kinematic sub-structure in the young sample.

2 PERIOD DETERMINATION

The SuperWASP project (Pollacco et al. 2006) is a wide-field photometric survey for transiting exoplanets that has been operating since 2004. The wide field of view of its two instruments located in La Palma (Spain) and South Africa (one set of eight Canon 200 mm f-1.8 lenses on each site, covering 482 deg^2 for each observatory and backed by high-quality 2048 $\times$ 2048 i-Kon CCD detectors) and typical observing cadence of $\sim$10 min also make it proficient at identifying many types of stellar variability with time-scales from one hour to several weeks. Data are available for tens of millions of objects with brightness in the approximate range $8 < V < 15$ covering most of the sky. An initial catalogue of objects was generated by cross-correlating the *ROSAT* sky-survey (1RXS) and pointed phase (2RXP) catalogues (Voges et al. 1999, see Section 5.3 for an analysis of the *ROSAT* data acquired in this work) with objects in the SuperWASP archive. We created a sample of 5477 stars using the criteria that SuperWASP targets must be within either the 3σ position uncertainty or 10 arcsec of the X-ray source (whichever was larger), have declinations $>-20^\circ$ and contain more than 1000 photometric data points in the archive up to the date 2010 July 20 when the data base query was performed.

Periodic variable stars were identified using the Lomb–Scargle periodogram technique described in Maxted et al. (2011). The Lomb–Scargle technique (Lomb 1976; Scargle 1982; Horne & Baliunas 1986; Zechmeister & Kürster 2009) searches for significant periodicities in unevenly sampled data. The SuperWASP light-curves are measured over several seasons of observation, each of which typically have $\sim$8000 unevenly sampled data points. To measure the period, we calculate the normalized power $P_n(\omega)$ at a given angular frequency, $\omega = 2\pi\nu$. The highest peaks in the calculated power spectrum correspond to candidate periodicities in the time series data. To obtain a solution for the light curve, a least-squares fit of the sinusoidal function $y_i = a\sin(\omega t_i) + b\cos(\omega t_i)$ to magnitudes $i = 1, 2, \ldots, N$ is found. A power spectrum is obtained based on a chi-squared fit of the light curve

$$P_n(\omega) = \frac{\chi_0^2 - \chi^2(\omega)}{\chi_0^2}, \quad (1)$$

where

$$\chi_0^2 = \sum \frac{m_i^2}{\sigma_i},$$

and

$$\chi^2(\omega) = \sum \frac{(m_i - y_i)^2}{\sigma_i^2}$$

To ensure the signal is not a noise artefact, the false alarm probabilities (FAPs) were calculated by making 100 permutations of each light curve using a bootstrap Monte Carlo technique developed by Collier Cameron et al. (2009). The FAP related to a given power P_n is taken as the fraction of randomized light-curves that have a highest power peak that exceeds P_n, which is the probability that a peak of a given height is merely caused by statistical variations, i.e. white noise. The spectrum of FAPs was used to estimate the power value in the periodogram for which this probability is 0.1, 1 and 10 per cent. Uncertainties are split into two separate error bars: first is the (averaged) measurement error using $\Delta P = \frac{\delta\mu P^2}{2}$ (equation 2 in Messina et al. 2010), where $\delta\mu$ is the finite frequency resolution of the power spectrum and is equal to the full-width half-maximum (FWHM) of the highest power peak in the frequency spectrum. The second error bar (where appropriate) is the standard error in two or more period measurements. Effects such as differential rotation between seasons may exceed any error bar generated from the width of the peak frequency, therefore errors based on only one season are likely to be underestimates (e.g. Reinhold, Reiners & Basri 2013; Epstein & Pinsonneault 2014). The error bars of objects with two seasons of data also risk underestimation because of the broad probability distribution of the standard error in two measurements.

Based on all the available periodograms, the periods were given a quality classification. If three or more seasons of data for an object resulted in an average period with a standard error smaller than 5 per cent they were graded as 'A'. To assess the period determination reliability, we measured the difference in χ^2 ($\Delta\chi^2$) between the second highest peak in each periodogram to the highest peak. If $\Delta\chi^2$, averaged over all observing seasons, was large enough (each light curve contains ∼8000 data points, so an average $\Delta\chi^2 > 1000$ was chosen as our minimum cut-off) and the value of the highest peak was larger than the FAP value at 0.1 per cent, we considered this a reliable period measurement. Objects with one or two seasons of data and satisfying the average $\Delta\chi^2$ criteria, and had a standard error smaller than 5 per cent were graded as 'B', whereas objects failing either the $\Delta\chi^2$ condition or resulting in large standard errors for their periods were graded 'C'.

From the initial catalogue of 5477 targets a sub-sample of 146 were chosen for spectroscopic investigation based on inspection of their light curves, period analysis, and their visibility during the observing run. Rapidly rotating, late-type stars with periods less than 5 d were considered for target selection. A sub-sample of 26 observed targets are listed in Table 1 (all other objects are listed in an online supplement). Note that for the purposes of this paper, the light curves were reanalysed using a larger data set (see Section 2) and nine of the redetermined periods were subsequently found to have periods >5 d.

We provide the raw light-curves, the periodograms and corresponding phase-folded light-curves for all objects that we obtained spectroscopy for (see Section 3.1) as an online supplement to this paper. A summary of the targets investigated in this paper and

Table 1. Measured periods for the sample of 26 likely-young objects (see Section 5.6). Periods are the reanalysed values (and standard errors) using the analysis in Section 2. The first error bar is the (averaged) uncertainty calculated using equation 2 in Messina et al. (2010). The second error bar (where appropriate) is the standard error in measurements for 2 or more seasons. '*N*' refers to the number of seasonal light-curves analysed for each target star. The column labelled '*Q*' refers to the quality of the period determination. The 'Date' column refers to the month and year when the first observation of the target in this work took place, J11 = June 2011, and D12 = December 2012. X-ray count rates (CR) and HR1 ratios are extracted from either the 1RXS or 2RXP catalogues and $\log L_X/L_{bol}$ is the X-ray to bolometric luminosity ratio. The equivalent data for all other objects observed in this work (and for all subsequent tabular data) are available online.

SuperWASP ID/Label (1SWASP J-)	V (mag)	$V-K_s$ (mag)	Period (d)	$\Delta\chi^2$	N	Q	Date	CR	HR1	$\log L_X/L_{bol}$
012457.96+255702.4, A	10.718	1.811	$3.048 \pm 0.120 \pm 0.026$	1711	2	B	D12	0.06	0.42	−3.35
013514.32+211622.4, B	10.788	1.490	$1.871 \pm 0.010 \pm 0.004$	1994	3	A	D12	0.01	1.00	−3.84
023503.81+313922.1, C	10.337	1.743	$1.274 \pm 0.013 \pm 0.002$	2038	4	A	D12	0.15	0.17	−3.18
030405.14+300309.6, D	10.875	1.807	$1.806 \pm 0.020 \pm 0.005$	1518	2	B	D12	0.06	0.66	−3.23
031628.14+563857.7, E	10.667	2.103	3.850 ± 0.080	584	2	C	D12	0.08	0.34	−3.31
032231.55+285319.8, F	10.672	2.013	$1.654 \pm 0.016 \pm 0.011$	281	2	C	D12	0.06	0.86	−3.34
034319.02+222657.2, G	11.571	2.545	2.893 ± 0.036	1075	1	B	D12	0.06	1.00	−3.07
050206.19+311102.2, H	10.792	2.218	4.531 ± 0.116	4169	1	B	D12	0.07	−0.07	−3.48
052146.83+240044.4, I	10.393	2.323	3.436 ± 0.054	9955	1	C	D12	0.30	−0.08	−3.01
084748.63+342356.8, J	10.304	1.686	4.231 ± 0.074	996	2	C	D12	0.03	−0.08	−3.90
133708.20+444454.5, K	11.050	1.954	4.376 ± 0.196	301	1	C	D12	0.07	−0.11	−3.32
135458.37−054354.1, L	9.231	2.091	$5.361 \pm 0.140 \pm 0.040$	319	2	C	D12	0.09	−0.60	−4.16
143854.57+330019.9, M	11.036	2.219	$5.095 \pm 0.156 \pm 0.036$	3576	2	B	D12	0.05	0.40	−3.36
162506.55+300225.8, N	10.205	3.022	$1.002 \pm 0.006 \pm 0.098$	51 786	2	B	D12	0.22	0.29	−3.27
214537.36+271110.8, O	11.425	2.305	$1.267 \pm 0.015 \pm 0.225$	1152	3	B	D12	0.06	0.29	−3.23
133241.69+223006.6, P	9.655	2.808	1.040 ± 0.013	186	1	C	J11	0.84	−0.13	−2.97
155007.38−022211.5, Q	10.050	2.538	$2.241 \pm 0.019 \pm 0.007$	37 160	3	A	J11	0.48	−0.09	−2.99
162946.59+281038.0, R	10.654	1.925	$1.426 \pm 0.011 \pm 0.003$	5023	4	A	J11	0.09	0.87	−3.14
171808.56+250612.0, S	10.614	3.027	$2.420 \pm 0.047 \pm 0.008$	5432	2	B	J11	0.27	0.04	−3.08
172228.64+365842.1, T	10.504	2.800	$1.229 \pm 0.011 \pm 0.001$	10 864	9	A	J11	0.25	−0.06	−3.14
173103.32+281506.5, U	10.213	2.402	$1.263 \pm 0.012 \pm 0.002$	13 828	3	A	J11	0.29	−0.05	−3.11
180426.56+393047.1, V	11.532	2.365	$1.547 \pm 0.017 \pm 0.004$	3260	5	A	J11	0.07	0.01	−3.15
192502.00+442950.7, W	9.939	2.398	$1.205 \pm 0.013 \pm 0.001$	11 141	2	B	J11	0.24	0.18	−3.23
205830.74−090223.3, X	11.180	2.071	$2.251 \pm 0.026 \pm 0.012$	5173	6	A	J11	0.11	0.28	−2.99
225617.59+205236.2, Y	11.410	2.731	$1.100 \pm 0.009 \pm 0.003$	1164	4	A	J11	0.08	0.06	−3.21
230752.70+171015.2, Z	10.780	2.881	$1.073 \pm 0.007 \pm 0.002$	980	3	C	J11	0.30	−0.25	−3.01

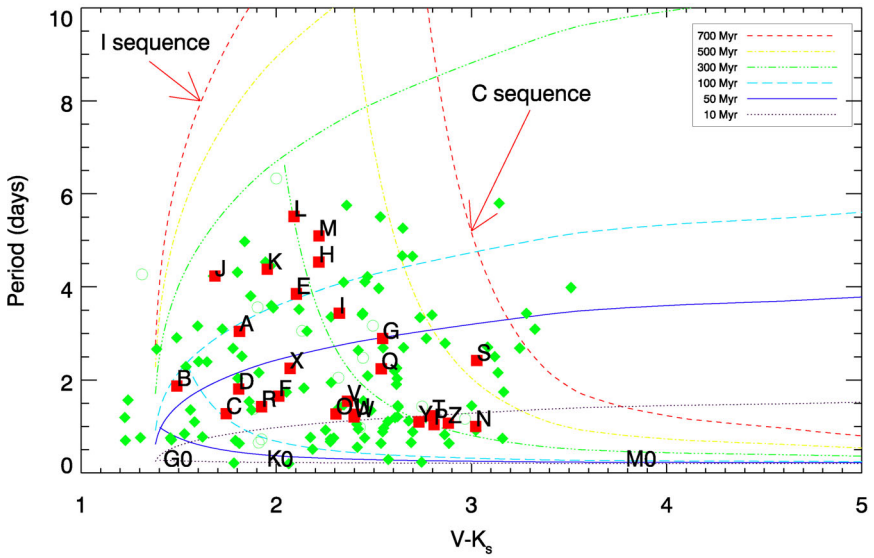

Figure 1. Rotation periods and $V - K_s$ colour for the entire observed sample. Red squares represent 26 objects that were later identified to be likely-young and were considered likely-single stars (referred to as the 'likely-young sample', see Section 5.6). All these objects are labelled from A to Z and their corresponding *ROSAT* 1RXS names are provided in Table 1. Any objects that had two or more separate RV measurements that varied by more than 5 km s^{-1} were assumed to be close-in short-period binaries and are denoted here by open green circles. All other objects are designated filled green diamonds. This symbol scheme for all other plots will remain the same throughout this work. The various lines represent the I- and C-sequence gyrochrones proposed by Barnes (2003) and calibrated by Mamajek & Hillenbrand (2008). The method of inferring an age range from the gyrochrones is described in Section 5.1 – note the three objects A, B and L which are used as examples to describe how to fit the age ranges.

their measured periods are provided in Table 1 along with their uncertainties and quality classification. Note that the light curves and the periods quoted in these tables are based on a reanalysis of all the SuperWASP data available up until 2012 December, performed after our spectroscopic follow-up. In most cases these agree with the original periods which were based on data up to the 2010 July 20; however, there are a handful of significant discrepancies.

The main source of B and V magnitudes are from the AAVSO All-Sky Photometric Survey (APASS; Henden et al. 2012), which covers the magnitude range $10 < V < 17$. All objects with V magnitudes <10 that were unavailable in the APASS catalogue were instead sourced from the NOMAD catalogue (Zacharias et al. 2005). All K magnitudes are from 2MASS (Cutri et al. 2003). Proper motions are extracted from the PPMXL catalogue of positions and proper motions (Roeser, Demleitner & Schilbach 2010). *BVK* photometry and proper motions are presented in Tables 4 and 6, respectively. Fig. 1 displays the entire observed sample plotted in terms of their rotation periods and $V - K_s$ colour.

3 SAMPLE SELECTION AND SPECTROSCOPIC OBSERVATIONS

3.1 Sample selection

Prior to selecting targets for spectroscopy, the light curves for the sample available in the SuperWASP catalogue were checked to identify objects most likely to be showing variability in their light curves as a result of starspot modulation. These were more likely to be objects with several seasonal light-curves. Whilst some objects had consistent periods measured from many seasons of data, with clear sinusoidal behaviour, some of the sample had sparse, poor-quality data and sometimes inconsistent period determinations. Because of the range of quality in data the selection process was entirely subjective. Any objects indicating a sharp dip in their light curve over any part of their phase were flagged as eclipsing binaries and discarded. The light-curve variability amplitudes were restricted to <0.2 mag and objects with measured periods to within a thousandth of either a half or integer number of days were discarded because they risked incorrect period determinations due to aliasing effects. Priority was given to objects where the profile of the multiseasonal light-curves significantly changed in shape; a strong indication of starspot migration over the course of several months.

The range of target spectral types is restricted to the range mid-F to early M (approximately $1.0 < V - K_s < 3.5$) for two reasons. First, because lithium is used as a primary youth indicator (see section 5.2), this range contains stars where significant and measurable Li depletion is expected on time-scales of 10–100 Myr (see Soderblom 2010 and references therein). The hot boundary is where Li-depletion time-scales become very long, and poorly understood diffusive or other non-standard mixing processes may become dominant (Boesgaard & Tripicco 1986). The cool boundary marks the point where Li depletion occurs extremely rapidly and even very young stars may have depleted their Li (e.g. Jeffries 2006). Secondly, low-mass MG stars will usually rotate very rapidly; FGK stars typically have spin-down time-scales of ∼50–100 Myr, and M-dwarfs ∼300 Myr or longer (this is illustrated by the gyrochrones in Fig. 1). Thus, fast rotation in M-dwarfs is not necessarily a sign of youth and the targeting of such objects could lead to high contamination with older stars. The basis for choosing our objects in terms of colour and rotation period is discussed in more detail in Section 5.1 where we use 'gyrochronology' to provide crude age estimates.

Objects in the SuperWASP catalogue may have correlated with *ROSAT* sources by random chance. To test this, the original

positions of all objects observed in the *ROSAT* catalogue were offset by 2 arcmin and checked again for neighbouring SuperWASP sources. The *ROSAT* error circles are about 10–20 arcsec, therefore a search radius of 15 arcsec was used to identify any neighbouring objects in the SuperWASP catalogue. Only one object (target W) out of 146 had a neighbouring SuperWASP source subsequent to being shifted by 2 arcmin. The chance of random correlation is 0.68 per cent.

An important point is that the nature of the target selection, from an all-sky survey, allows for a *kinematically unbiased* sample, independent of proper-motion or RV criteria. This provides an opportunity to identify young stars that do not share the galactic space motions of previously identified MGs. The sample is not spatially unbiased, because the SuperWASP survey avoids galactic latitudes between $\pm 20^{\circ}$.

3.2 Observation strategy

We obtained high-resolution multi-echelle spectroscopy of 146 objects over 2 telescope runs using the Fibre-fed Echelle Spectrograph (FIES) on the 2.56 m NOT at the Roque de los Muchachos Observatory. Our first observing run of 68 targets lasted four consecutive nights from 2011 June 21, and a further 78 targets were observed on 2012 December 27, 28 and 29. FIES was used in medium resolution mode ($\lambda/\Delta\lambda = 46\,000$). Each target observation was bracketed with short ThAr arc lamp exposures to provide a wavelength calibration. In what follows, objects observed in 2011 June or 2012 December are denoted J11 and D12, respectively (these are listed in the 'Date' column in Table 1).

Our observing strategy was to obtain a single observation of a target, reduce the data in real time at the telescope and inspect the spectrum for the presence of the Li I 6708 Å doublet. If Li was clearly present then, if necessary, a further exposure was performed to obtain a signal-to-noise ratio (SNR) per pixel of $\geq$50 around the Li line. Objects where Li was detected were observed again on a subsequent night in order to check for short-term RV changes that might betray their close binary nature (see Section 4.5 for further details on binary contaminants in the survey).

The real time data reduction at the telescope and subsequent reduction at Keele University were accomplished using the FIESTOOL package created by Eric Stempels. This package performed bias, blaze and flat-field corrections, optimal extraction of the spectra and wavelength calibration using the adjacent arc lamp exposures. With fibre bundle #3, FIES covers a spectral range of λλ 3630–7260 Å over 78 spectral orders. Observations were also made of several RV and low-activity template stars (selected for their extremely low levels of chromospheric Ca II H and K emission) over a similar spectral-type range as the targets. These were used to calibrate RVs and projected rotational velocities ($v \sin i$) and are listed in Table 2.

To further identify whether or not objects were short-period binaries, several of the most probable young objects were later re-examined using long-slit spectroscopy on the INT on 2013 March 23 and 24, in combination with the H1800V grating and IDS-235 wide-field camera. This allowed for an RV precision of $\sim$1–2 km s^{-1} and these measurements were compared to the RVs measured at the NOT. In this work, the RV measurements at the INT are not incorporated into the final averaged RV, rather they are used to check for RV consistency and Li content. All individually measured RVs are presented in column 3 of Table 3 and INT observations are subscripted with an 'i'.

Table 2. RV and minimum activity standards – All RV are from Chubak et al. (2012), except for HD 114762 (Udry, Mayor & Queloz 1999). All $v \sin i$ values are from Glebocki & Gnacinski (2005). All log $R'_{\rm HK}$ are from Isaacson & Fischer (2010), except for HD 3651 (Pace 2013) and HD 190007 (Mittag et al. 2011).

Standard	SpT	RV (km s^{-1})	$\sigma_{\rm RV}$ (km s^{-1})	$v \sin i$ (km s^{-1})	log $R'_{\rm HK}$
HD 114762	F8V	49.4	0.5	1.7	−4.902
HD 1461	G0V	− 10.158	0.116	5.0	−5.008
HD 95128	G1V	11.293	0.108	3.1	−4.973
HD 217014	G2.5IVa	− 33.118	0.128	2.8	−5.054
HD 197076	G5V	− 35.402	0.030	2.9	−4.872
HD 9407	G6V	− 33.313	0.124	0.0	−4.986
HD 115617	G7V	− 7.844	0.128	0.5	−4.962
HD 101501	G8V	− 5.464	0.105	2.3	−4.483
HD 3651	K0V	− 32.940	0.042	0.6	−4.849
HD 10780	K0V	2.814	0.086	0.9	−4.700
HD 131509	K0V	− 44.749	0.167	6.4	−5.142
HD 4628	K2.5V	− 10.229	0.030	1.6	−4.979
HD 190007	K4Vk	− 30.270	0.105	2.8	−4.592
HD 209290	M0V	18.275	0.120	3.8	
HD 119850	M1.5V	15.778	0.061	1.8	
GJ 411	M2.0V	− 84.683	0.030	1.6	
GJ 526	M4.0V	15.778	0.061	1.8	

4 DATA ANALYSIS AND RESULTS

4.1 Equivalent widths (EWs)

Li EWs were estimated from the NOT spectra using the SPLOT procedure in IRAF.[1] Lines were measured by manual integration, where the linear continuum is subtracted and pixels were summed with partial pixels at the ends to obtain a flux. Although the Li line at 6707.8 Å actually consists of two neighbouring lines at λλ 6707.761, 6707.912 Å our spectroscopy cannot resolve these lines. There is also a contaminating weak Fe I spectral line at 6707.441 Å blended into the Li resonance line. Where necessary, we use a correction for this blend, $W_\lambda(\text{blend}) = 20(B-V) - 3$ mÅ provided in Soderblom et al. (1993d). EW measurement errors were estimated using the procedure highlighted in Cayrel de Strobel & Spite (1988):

$$\delta\text{EW} = 1.6 \times \sqrt{\text{FWHM} \times p}/\text{SNR}, \quad (2)$$

where FWHM refers to the observed full width half-maximum (in Å) of the line, and p is the pixel size (0.113 Å). The SNR was calculated empirically from the rms of fits to continuum regions.

Measurements of the 6563 Å H α line EW were made by direct integration above a surrounding pseudo-continuum. We provide both Li and H α EW measurements in Table 4.

4.2 Radial velocities

We used the FXCOR procedure in IRAF, which cross-correlates pixels between the target objects and those of template spectra to determine a relative RV (Tonry & Davis 1979). SNR improves towards the red end of the spectrum, therefore measurements were made over nine consecutive orders (λλ 5920–6520 Å), avoiding the broad Na D lines and contamination from telluric absorption. To determine the

[1] IRAF is distributed by the National Optical Astronomy Observatory, which is operated by the Association of Universities for Research in Astronomy (AURA) under cooperative agreement with the National Science Foundation.

Table 3. RV measurements. Individual RVs are provided in column 3 and the final averaged RV in column 4. The INT RV measurements are subscripted with an 'i' and are not factored into the final averaged RV for each target. The column titled '*B*' is the binary score based on the criteria described in Section 4.5.

Target	HJD (2450000+)	RV_{indiv} ($km\,s^{-1}$)	RV_{final} ($km\,s^{-1}$)	*B*
A	6289.422	7.2 ± 0.7	7.3 ± 0.7	1
	6290.409	7.4 ± 0.7		
B	6289.358	5.0 ± 1.9	5.0 ± 2.0	1
	6290.427	5.0 ± 2.2		
C	6289.370	0.3 ± 2.5	0.3 ± 2.4	1
	6290.442	0.2 ± 2.3		
D	6289.476	9.8 ± 2.4	9.8 ± 2.4	1
	6290.448	9.8 ± 2.4		
E	6289.488	−2.0 ± 0.6	−2.1 ± 0.6	1
	6290.460	−2.1 ± 0.6		
F	6289.498	8.2 ± 1.8	9.0 ± 1.8	1
	6290.469	9.9 ± 1.9		
G[a]	6291.569	6.0 ± 0.5	6.0 ± 0.5	1
H	6291.589	11.2 ± 0.6	11.2 ± 0.6	1
	6376.436	$14.2 \pm 2.2_i$		
I[b]	6291.598	13.5 ± 0.5	13.5 ± 0.5	1
	6376.429	$17.1 \pm 2.2_i$		
J	6289.580	10.1 ± 0.6	10.2 ± 0.6	1
	6290.617	10.2 ± 0.6		
	6375.474	$11.6 \pm 1.5_i$		
K	6289.720	−6.4 ± 0.6	−6.4 ± 0.6	1
	6290.708	−6.4 ± 0.6		
	6375.619	$-1.2 \pm 3.5_i$		
L	6289.731	−4.1 ± 0.6	−4.2 ± 0.6	1
	6290.719	−4.2 ± 0.6		
	6375.631	$-2.3 \pm 1.6_i$		
M	6289.738	−19.2 ± 0.6	−19.2 ± 0.6	1
	6291.634	−19.3 ± 0.6		
N	6289.780	−68.0 ± 0.7	−68.5 ± 0.7	1
	6290.791	−69.1 ± 0.7		
O	6290.317	−22.5 ± 1.8	−22.9 ± 1.6	1
	6291.314	−23.4 ± 1.4		
P	5735.502	−5.1 ± 0.7	−5.1 ± 0.7	1
	6375.594	$-5.0 \pm 2.2_i$		
Q[c]	5736.457	−10.3 ± 0.3	−10.6 ± 0.4	1
	5737.503	−10.9 ± 0.4		
	6375.688	$-10.4 \pm 2.3_i$		
R	5735.567	−25.3 ± 0.8	−25.2 ± 0.8	1
	5736.515	−25.1 ± 0.7		
	6375.699	$-20.3 \pm 2.2_i$		
S	5736.483	−34.7 ± 0.3	−34.8 ± 0.3	1
	5737.513	−34.9 ± 0.3		
T	5735.613	−24.6 ± 0.6	−25.3 ± 0.6	1
	5736.524	−26.0 ± 0.6		
U	5735.643	−18.2 ± 0.5	−18.2 ± 0.5	2
V	5736.591	−25.5 ± 0.6	−26.4 ± 0.6	1
	5737.569	−27.3 ± 0.7		
W[d]	5734.615	−33.5 ± 0.6	−33.5 ± 0.6	1
X	5736.652	−3.0 ± 0.4	−2.7 ± 0.4	1
	5737.617	−2.4 ± 0.4		
Y	5737.676	−2.5 ± 0.6	−2.5 ± 0.6	2
Z	5737.662	−8.4 ± 0.3	−8.4 ± 0.3	2

[a] RV = 6.06 ± 0.29 $km\,s^{-1}$ (Mermilliod, Mayor & Udry 2009), [b] RV = 14.2 ± 1.4 $km\,s^{-1}$ (Biazzo et al. 2012), [c] RV = −13.6 ± 1.8 $km\,s^{-1}$ (Kordopatis et al. 2013), [d] RV = −33.1, −33.1, −32.2 $km\,s^{-1}$ (Frasca et al. 2011).

centre of the cross-correlation function (CCF) peak a Gaussian fit was made to pixels within the top 40 per cent of the normalized peak. Some orders match better than others and poor CCF matches could be due to a spectral-type mismatch between an RV standard and a target, too much noise in the data, or, if the target is a close binary, then the CCF may contain multiple (unresolved) peaks. The spectrum of a binary companion could be blended and more apparent in some orders than others. In some cases, no CCF peak was observed at all. In order to provide a more robust RV measurement (and also assess the precision) the clipped mean RV from nine orders. Any measurements $>2\sigma$ from the mean were removed, and the process iterated a maximum of 10 times. A weighted average relative RV for each target was calculated over each order for each template star using the *R* quality factor in Tonry & Davis (1979).[2] In all cases the template that provided the lowest error in RV was used. Finally, the RVs were transferred on to a heliocentric reference frame.

There were three sources of error: the standard error measured over the echellogram orders (weighted by *R*), the published RV uncertainty of the standard star used in the calibration and a systematic uncertainty estimated from the cross-correlations of all the RV standards with one another. These errors were treated as independent and were added in quadrature. RV measurements and errors are provided in Table 3, along with any previous literature values. The RV measurements for each RV standard relative to one another formed a matrix of cross-correlation values. The systematic uncertainty was measured to be 0.36 $km\,s^{-1}$ for the templates used in the 2011 June run and 0.27 $km\,s^{-1}$ for the templates used in the 2012 December run. To avoid any spectral mismatch between target and template calibrations, templates are restricted to within 0.5 spectral classes of the target star in each case. RVs obtained from INT spectroscopy were measured using a similar procedure, but this time separating the long-slit spectra into ten 50 Å windows between 6600 and 7100 Å and obtaining the mean RV, weighted by *R*. These measurements were not included in the final averaged RV, however because the overall accuracy was much poorer, limited by systematic uncertainties of $\sim$1 $km\,s^{-1}$ in the wavelength calibration, were used only to support the data obtained from the NOT.

From the initial sample of 146 targets, 28 were found to have indeterminate RVs (as a result of poorly constrained cross-correlation peaks due to noisy data, high $v \sin i$ or perhaps binarity) and 14 objects were observed to have RVs that varied by more than 5 $km\,s^{-1}$ on the time-scale of the observing run, presumably as a result of binarity (see Section 4.5).

4.3 Projected rotational velocities

Projected rotational velocities ($v \sin i$) were estimated from the FWHM of the CCF using a set of simulations for objects observed on the NOT. Broadened versions of a number of slowly rotating template stars ($v \sin i$ templates, see Table 2) were produced by convolving high SNR spectra ($\simeq$100) with a rotational broadening convolution kernel, using a limb-darkening parameter $\epsilon = 0.6$. Because the $v \sin i$ templates all had a small, but finite, rotational speed (<5 $km\,s^{-1}$) a correction was made for the small measured $v \sin i$ values of the standards to set their non-rotating profiles at zero, and artificial Gaussian noise was injected into the spun-up spectra. For stars with large rotational broadening, the high-frequency (wavenumber $k > 400\,m^{-1}$) components in the spectra were filtered

[2] This is the ratio of the height of the true peak in the CCF compared to the average CCF value over the whole spectral order.

Table 4. EWs, *BVK* photometry, temperatures, spectral types (SpT) and Li abundances. Li EW_c is the final EW after correcting for the blended Fe I line.

Target	Li EW (mÅ)	Li EW_c (mÅ)	H α EW (Å)	B (mag)	V (mag)	K_s (mag)	T_{eff} (K)	SpT	A(Li)
A	223	213 ± 13	1.28	11.470 ± 0.045	10.718 ± 0.042	8.907 ± 0.019	5430	G9	$2.89^{+0.09}_{-0.13}$
B	154	144 ± 21	2.22	11.387 ± 0.008	10.788 ± 0.020	9.298 ± 0.016	5850	G1	$2.91^{+0.10}_{-0.14}$
C	209	197 ± 20	0.99	10.980 ± 0.061	10.337 ± 0.049	8.594 ± 0.017	5510	G8	$2.88^{+0.11}_{-0.15}$
D	193	186 ± 21	1.77	11.579 ± 0.087	10.875 ± 0.076	9.068 ± 0.018	5440	G8	$2.77^{+0.14}_{-0.18}$
E	222	211 ± 13	0.82	11.482 ± 0.049	10.667 ± 0.023	8.564 ± 0.020	5120	K1	$2.59^{+0.08}_{-0.12}$
F	184	174 ± 25	0.71	11.356 ± 0.050	10.672 ± 0.059	8.659 ± 0.019	5210	K1	$2.52^{+0.13}_{-0.18}$
G	267	246 ± 25	0.49	12.537 ± 0.056	11.571	9.026 ± 0.020	4710	K4	$2.35^{+0.10}_{-0.18}$
H	249	238 ± 16	0.80	11.671 ± 0.078	10.792 ± 0.017	8.574 ± 0.021	5000	K2	$2.61^{+0.08}_{-0.13}$
I[a]	386	366 ± 14	− 0.05	11.367 ± 0.045	10.393 ± 0.043	8.070 ± 0.021	4900	K3	$3.18^{+0.09}_{-0.14}$
J	165	155 ± 15	1.83	10.958 ± 0.023	10.304 ± 0.038	8.618 ± 0.022	5590	G6	$2.76^{+0.10}_{-0.14}$
K	260	245 ± 10	1.07	11.852 ± 0.027	11.050 ± 0.022	9.096 ± 0.018	5270	K0	$2.89^{+0.07}_{-0.11}$
L	169	159 ± 12	1.98	10.089 ± 0.144	9.231 ± 0.104	7.140 ± 0.020	5130	K1	$2.38^{+0.15}_{-0.19}$
M	106	93 ± 8	0.96	11.934 ± 0.055	11.036 ± 0.048	8.817 ± 0.020	5000	K2	$1.92^{+0.11}_{-0.14}$
N	86	69 ± 15	− 0.40	11.311 ± 0.032	10.132 ± 0.037	7.183 ± 0.027	4710	K5	$1.95^{+0.14}_{-0.19}$
O	254	242 ± 24	− 0.08	12.014 ± 0.032	11.279 ± 0.037	9.120 ± 0.018	5060	K2	$2.68^{+0.11}_{-0.17}$
P[b]	159	142 ± 14	− 0.62	10.669 ± 0.043	9.655 ± 0.024	6.847 ± 0.023	4390	K5	$1.07^{+0.10}_{-0.15}$
Q	174	155 ± 23	− 0.01	10.939 ± 0.041	10.050 ± 0.058	7.512 ± 0.023	4490	K5	$1.65^{+0.13}_{-0.18}$
R	208	196 ± 18	1.14	11.394 ± 0.062	10.654 ± 0.041	8.729 ± 0.020	5300	K0	$2.70^{+0.11}_{-0.15}$
S	135	117 ± 4	− 1.22	11.533 ± 0.184	10.614 ± 0.069	7.587 ± 0.020	4330	K6	$1.31^{+0.12}_{-0.12}$
T	62	44 ± 7	− 0.34	11.601 ± 0.046	10.504 ± 0.039	7.704 ± 0.017	4500	K5	$1.01^{+0.12}_{-0.16}$
U	278	265 ± 36	0.19	11.069 ± 0.026	10.213 ± 0.011	7.811 ± 0.016	4830	K3	$2.58^{+0.15}_{-0.25}$
V	269	252 ± 36	− 0.18	12.603 ± 0.066	11.532 ± 0.046	9.167 ± 0.017	4860	K3	$2.63^{+0.17}_{-0.26}$
W[c]	222	208 ± 20	0.01	11.011 ± 0.047	9.939 ± 0.061	7.541 ± 0.018	4840	K3	$2.31^{+0.12}_{-0.17}$
X	337	279 ± 42	0.76	12.208 ± 0.252	11.180 ± 0.112	9.109 ± 0.021	5150	K1	$2.93^{+0.23}_{-0.29}$
Y	141	122 ± 8	− 0.36	12.390 ± 0.071	11.410 ± 0.072	8.679 ± 0.016	4560	K4	$1.62^{+0.13}_{-0.17}$
Z	163	146 ± 30	− 1.50	11.867 ± 0.054	10.780 ± 0.024	7.899 ± 0.027	4440	K5	$1.60^{+0.14}_{-0.21}$

[a] H α EW = −2.14 Å; Li EW = 390 mÅ(Li & Hu 1998). H α EW = −4.00 Å; Li EW = 350 mÅ, [b] H α EW = 0.6 Å (Mason et al. 1995), [c] $\log g = 4.39$; [Fe/H] = −0.01 (Pinsonneault et al. 2012).

out to minimize the effects of Gaussian noise (and the same filtering also applied to the target spectra). Each standard was broadened in 1 km s^{-1} steps between 5 and 70 km s^{-1} and the FWHM of each broadened standard cross-correlation peak was recorded using FXCOR and repeated for the same echellogram orders used in the RV analysis. Relationships between FWHM of the CCF and $v \sin i$ were derived using the means from the orders weighted by the R quality factor (see Tonry & Davis 1979) for each template. To ensure there were no spectral mismatches, only $v \sin i$ template spectra within five spectral sub-classes of the target were used in each case. The resolving power and SNR for spectra on the INT were insufficient to obtain $v \sin i$ measurements. The measured $v \sin i$ values are presented in Table 6.

4.4 Effective temperatures and Li abundance calculations

Effective temperatures were estimated based on a fifth-order polynomial interpolation of the $V - K_s$ and T_{eff} values between F0 and M3 stars provided in table 5 of Pecaut & Mamajek (2013) and spectral types are calculated from their linear interpolation with $V - K_s$ in the same table. There is evidence to suggest that the metallicities of young, nearby stars do not vary much from the solar value (Spina et al. 2014) and FGK stars should be close to the Zero-Age Main Sequence (ZAMS) by 20 Myr. The EW of the Li I 6708 Å line is transformed into logarithmic Li abundances (on the usual scale where $\log N(H) = 12$) using the curves of growth from Soderblom et al. (1993c) and correcting for non-local thermodynamic equilibrium effects using the code provided in Carlsson et al. (1994). Table 4 displays the temperatures, EWs, Li abundances and their associated uncertainties.

4.5 Binary contaminants

Tidally-locked, short-period binaries (herein, TLSPBs) maintain high rotational velocities well into their main-sequence lifetimes and therefore can retain short rotation periods into old age. According to numerical calculations, solar-mass binaries starting from the birthline that have periods $\lesssim$8 d will have circular orbits and synchronous rotation upon reaching the main sequence (Stahler & Palla 2005). They will not spin-down with age like single stars, but their rapid rotation will ensure they maintain their magnetic activity levels. Furthermore, there is evidence that TLSPBs may deplete their lithium at a different rate to single stars (e.g. Barrado y Navascués, Deliyannis & Stauffer 2001; Canto Martins et al. 2011; Strassmeier et al. 2012). For these reasons we attempt to identify these objects in our sample and when we find them we do not attempt to estimate their age.

TLSPBs are expected to be the main contaminants in our survey, but should have large RV variations detectable by two observations separated by ∼24 h. In general, the RVs of likely-single, slow rotators with a reasonable SNR could be measured to a precision of ∼1 km s^{-1}. We set a criterion that an RV difference >5 km s^{-1} between two measurements of the same object on separate nights identifies these objects as close binary systems. A numerical grading system is used to distinguish likely single stars (allocated a grade of 1) from those very likely to be binaries (allocated a grade of 5). A score of 5 was given if we detected RV differences >5 km s^{-1} for a target on separate nights or (if there was only one measurement) if there were literature sources indicating that either the object is a close binary or report a RV measurement >5 km s^{-1} discrepant from our measurement. In addition, to score 5, the average error in RV measurement must be less than 5 km s^{-1}. Objects are graded 4 if there is only one spectrum which results in (a) a clear, multipeaked CCF and (b) an RV error <5 km s^{-1}. A grade of 3 was given if the status of the star from the CCF was unclear (presumably as a result of poor SNR and/or large $v \sin i$), resulting in either an indeterminate RV or a RV uncertainty >5 km s^{-1}. A grade of 2 was used for objects which had a single spectrum, an RV uncertainty <5 km s^{-1} and a distinct single peak in the CCF. Finally, objects scoring 1 had consistent, low-uncertainty RV measurements for 2 or more spectra. Individual RV measurements and binary scores for each object are presented in Table 3.

From the entire observed sample of 146 objects, 14 scored 5, 29 of them scored either 4 or 3, 45 scored 2 and 29 objects scored 1. Any objects that scored 5 were automatically assumed to be close binaries. All targets selected for further analyses in Section 7 have binary scores of either 1 or 2. However, 2 or more consistent RV values for an object is not a guarantee that the object is not a TLSPB. Given that some of the objects in this sample have orbital periods of the order of ∼24 h, consistent RV measurements could be a result of measuring two points at the same phase on an RV curve.

4.6 Binary simulation

Although the criterion that two separate observations resulting in RV differences >5 km s^{-1} is sufficient to flag these objects as TLSPBs, a fraction with RV differences <5 km s^{-1} may remain undetected. In a TLSPB system the rotation period will be equal to the orbital period. Given that these observations are incapable of distinguishing between TLSPBs and single stars, a simulation was carried out to calculate the probability that each object showing no RV variations (i.e. not >5 km s^{-1}) was in fact a short period binary seen at low inclination or at two similar phases in its orbit.

The simulation used 10^6 iterations, a flat mass-ratio between 0.20 and 0.95 (Hogeveen 1990) and the primary mass was estimated from its spectral-type. Tidally-locked binaries will be circular, therefore the eccentricity is zero in all calculations. A value between 0 and 2π was randomly assigned for the argument of periastron. A second RV measurement was calculated at a later time equal to the cadence (cad) between observations.

We carried out the simulation for all objects that had two separate RV measurements at the NOT. In some cases, the separation between the observations was similar to an integer number of rotation periods. In these cases, a TLSPB nature cannot be ruled out with any confidence but for the majority of cases we are ∼90 per cent confident that they cannot be TLSPBs. In other words in >90 per cent of the simulations there would have been a ΔRV > 5 km s^{-1}. Simulations for two objects, target P (P = 1.04 d, cad = 2.00 d, the probability that the object is a TLSPB ($P_{\rm TLSPB}$) = 0.12) and target D (P = 3.85 d, cad = 0.97 d, $P_{\rm TLSPB}$ = 0.15) are presented in Fig. 2. In the initial target selection, light curves indicative of eclipsing binaries were filtered out, therefore it is unlikely that high inclination, eclipsing TLSPBs have been included. For example, a 0.7 $M_\odot$/0.5 $M_\odot$ binary system with an orbital period of 3 d would be at least partially eclipsing if the inclination angle, $i > 60°$. Given a random orientation of orbital rotation axes, the probability of observing an object with $i > 60°$ is 0.5, therefore $P_{\rm TLSPB}$ could be overestimated by a factor of 2.

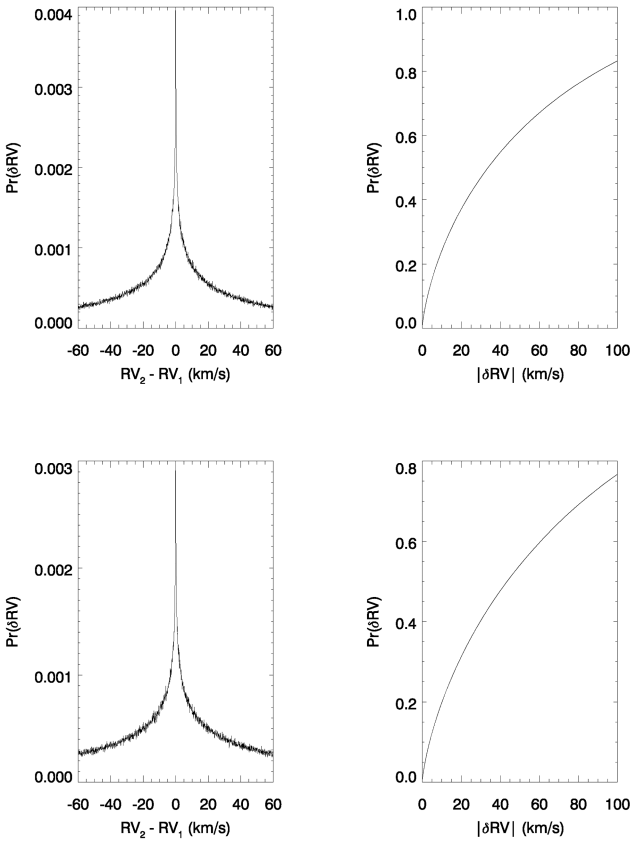

Figure 2. Simulations to calculate the fraction of tidally-locked binary objects that would result in an RV difference <5 km s^{-1} over the cadence of two observations for target D (top) and target P (bottom). The input parameters and a description of the simulation is provided in Section 4.6. The left-hand panel demonstrates the probability that a binary star has a particular RV difference of a certain value. The right-hand panel is the cumulative probability that an object has $|RV_2 - RV_1|$ less than a given value.

The incidence of close binaries in a random sample of field stars is expected to be quite low. We simulated a field population based on the binary fraction, period and eccentricity distribution of field solar-type stars proposed by Raghavan et al. (2010), finding that only 2.2 per cent of such a sample should lead to observed RV differences of >5 km s^{-1} in observations separated by ∼1 d. However, of the 55 objects that we observed twice, 11 were found to show evidence of close binarity – significantly higher than 2.2 per cent. The reason is likely that we are not observing random field stars, but a sample of fast-rotating, active stars, which will tend to be either young or in close binary systems (e.g. Jeffries 1995).

The field star simulation served an additional purpose. Where we identify a Li-rich, potentially young star, with two consistent RV measurements (within 5 km s^{-1}), then assuming that these stars share the same binary properties as average field stars, there is still

a 7.2 per cent probability that the true systemic velocity could be different to that measured by $>5\,\mathrm{km\,s^{-1}}$ due to the presence of an unseen or unresolved wide binary companion.

5 FINDING YOUNG STARS

5.1 Gyrochronology

Gyrochronology provides a colour-dependent method to obtain an age estimate for single, late-type stars by using empirical fits to rotation rates in open clusters of known age. Fig. 1 displays the rotation periods against $V - K_s$ for the entire observed sample, overplotted with curves for the interface (I) and convective (C) sequences of the form defined by in Barnes (2003; 2007). Mamajek & Hillenbrand (2008) find age discrepancies between the calibrated gyrochrones in Barnes (2003; 2007), claiming that the Barnes calibrations would underestimate the Hyades age. We therefore use the updated calibration in Mamajek & Hillenbrand (2008) and transform $B - V$ to $V - K_s$ by interpolating table 5 in Pecaut & Mamajek (2013). At this point we stress two issues about our use of gyrochronology; first, the calibrations in Mamajek & Hillenbrand (2008) are for stars with $0.5 \leq (B - V)_0 \leq 0.9$ (∼F7–K2) and roughly half of our sample are redwards of this range. Secondly, we find that in almost all of our sample the upper age limits are not generally affected by the choice of either the Barnes (2007) or Mamajek & Hillenbrand (2008) calibrations.

The bifurcation point is the point at which the C sequence meets the I sequence and the isochrones become bimodal redwards of this point. To estimate an age using gyrochronology, the following analysis is carried out (see Fig. 1).

(i) If the object lies above the I sequence, it is definitely older than this gyrochrone.

(ii) If the object lie below the I sequence and bluewards of the corresponding C sequence, then this target is younger than that gyrochrone.

(iii) If the object lies below the I sequence and redwards of the corresponding C sequence, there is an ambiguity and one must look for an older gyrochrone which satisfies the previous condition.

To clarify how gyrochronology works in practice, we highlight three stars from Table 1 (targets A, B and L).

Target A – Target A lies below the 100 Myr I sequence, but above the 50 Myr I sequence. It is redwards of the 10, 50 and 100 Myr C gyrochrones, but lies bluewards of the 300 Myr C gyrochrone and the 300 Myr bifurcation point. Hence the age of target A is estimated to be <300 Myr, with a lower limit of 50 Myr.

Target B – Target B has a minimum age of 50 Myr, as it lies above the I sequence of this isochrone. It is below the I sequence of all gyrochrones with ages ≥100 Myr but is only bluewards of the C sequence for those with ages ≥100 Myr. Hence the age of B is estimated to be between 50 and 100 Myr.

Target L – Target L is at least older than 100 Myr, because it is above the I sequence at this age. Although it lies below all the I sequences ≥100 Myr it is only bluewards of the C sequence at an age of 300 Myr. Hence L has a gyrochronology age between 100 and 300 Myr.

The limitations of the initial target selection in terms of colour and period now become clearer when examining Fig. 1. A period <5 d implies an age <700 Myr for F-stars; <300 Myr for G-stars with $1.5 < V - K_s < 2.0$, but then increases again to <700 Myr for K-stars with $2.0 < V - K_s < 3.0$ and even older for M-dwarfs. Reversing this argument, to be sure an object has an age ≤100 Myr would require it to have a period of <1 d if it were a late F-star, <2 d for a G-star and then less than 0.7 of a day for K-stars and less than 0.3 of a day for M-stars. To avoid ambiguity with interpreting the C-sequence, we provide (and employ) only upper-age limits from gyrochronology for the likely-young sample and these are provided in Table 5.

Table 5. Age estimates in Myr for the entire observed sample, based on Gyrochronology, H α, Li EW and $R \sin i$/colour. The final age estimate is solely from the Li EW age, other age indicators are used only as supporting evidence for the Li age.

Target	Gyro (Myr)	Li EW (Myr)	H α (Myr)	$R \sin i$ (Myr)
A	<300	30–150	>21	
B	<100	30–200	>17	
C	<100	30–200	>20	
D	<300	30–200	>21	
E	<300	30–200	>27	
F	<300	30–200	>24	
G	<500	30–150	>41	
H	<500	30–150	>32	
I	<500	5–30	35–50	
J	<300	30–150	>19	
K	<300	30–150	>22	
L	<300	30–150	>27	
M	<500	100–200	>32	<5
N	<500	30–150	<189	
O	<300	30–150	29–39	
P	<300	30–150	66–127	
Q	<500	30–150	41–64	
R	<300	30–150	>22	
S	<700	30–150	<233	<80
T	<500	100–200	<123	
U	<300	30–150	>37	
V	<300	30–150	<53	
W	<300	30–150	37–55	<80
X	<300	30–150	>26	
Y	<300	30–150	<99	
Z	<500	30–150	<158	

Gyrochronology will not work for tidally-locked binary systems. Because this is the likely status of all the objects flagged as 4 or 5 in the binarity tests, we choose not to assign ages to them based on gyrochronology (or activity – see Section 5.4).

5.2 Li EW measurements compared to known clusters

The strength of photospheric lithium in cool stellar atmospheres can be used as an empirical age indicator. Stars are born with the Li abundance of the interstellar medium, but it is depleted by proton capture in their interiors. Mixing processes bring the Li-depleted material to the surface, resulting in an age- and mass-dependent photospheric Li-abundance (see Sestito & Randich 2005; Jeffries 2006).

Whilst theoretical models partially capture the behaviour of PMS Li depletion in FGK stars, they are strongly sensitive to the assumed opacities in the atmospheres and interiors of these stars and cannot readily explain the spread in Li abundance that is seen at a given effective temperature in presumably coeval clusters. For example, the spread in Li abundance amongst K-stars in the Pleiades is 1–2 dex (Soderblom et al. 1993b). For these reasons Li is used here only

as an empirical age estimator by comparing the Li EWs of targets, as a function of $B - V$ and $V - K_s$ (or equivalently, Li abundance versus $T_{\rm eff}$), with stars observed in the Hyades (age ∼625 Myr, Perryman et al. 1998) and Pleiades (age ∼125 Myr; Stauffer, Schultz & Kirkpatrick 1998) clusters. Li EW data obtained from Soderblom et al. (1990, 1993b,c,d, 1995a,b), Jones et al. (1996, 1997), Jones, Fischer & Soderblom (1999), Soderblom et al. (1999) and Wilden et al. (2002). In addition, comparisons were made with three younger clusters; NGC 2264 (age ∼5 Myr; King 1998; Soderblom et al. 1999; Dahm & Simon 2005), γ Vel (age ∼10 Myr; Jeffries et al. 2014) and IC 2602 (∼30 Myr; Meola et al. 2000; Randich et al. 2001; Randich 2001).

In Fig. 3, we present the Li EWs and colours for the entire observed sample, and ages are estimated using comparisons to the Li patterns in the aforementioned open clusters. One object (labelled as target I) with duplicate, consistent RV measurements has a Li EW/$V - K_s$ indicative of stars younger than the Pleiades (more similar to the pattern observed in γ Vel at ∼10 Myr). A further 25 targets with binary scores of 1 or 2 have Li EWs/colours (or Li abundances/temperatures) consistent with the Pleiades or IC 2602. The remainder of the targets appear to have depleted their Li sufficiently that they appear older than the Pleiades, or they are close binaries and their Li-depletion may not properly reflect their true age. There is some evidence that close binary system components have anomalous Li-depletion histories (see, for example Strassmeier et al. 2012). The bottom plot of Fig. 3 is A(Li) versus $T_{\rm eff}$. As this is essentially the data from the top two plots of Fig. 3 folded through a transformation, it contains no new information on the ages, but does illustrate that the most Li-rich stars found are still depleted from an assumed initial level of about A(Li) = 3.3, so are probably not very young PMS stars. The estimated Li age ranges for the entire observed sample are presented in Table 5.

5.3 X-ray activity in the *ROSAT* catalogue

The initial selected targets described in Section 3 were chosen based on their short rotation periods and assessment of apparent rotation modulation in their light curves. All such objects originated from a catalogue of objects that had entries in both *ROSAT* and SuperWASP. Throughout the selection process no criteria were used based on any specific X-ray property – a data base entry in either the 1RXS or 2RXP catalogue was deemed sufficient. Data were available for all the selected targets and were analysed subsequent to the telescope observations. $L_{\rm X}/L_{\rm bol}$ was calculated for each object using the following formula:

$$\frac{L_{\rm X}}{L_{\rm bol}} = \frac{f_{\rm X}}{2.48 \times 10^{-5} \times 10^{-0.4 m_{\rm bol}}}. \quad (3)$$

The *ROSAT* catalogues were revisited to obtain count rates, exposure times and hardness ratios (CR, exp and HR1, respectively, all provided in Table 1). X-ray fluxes ($f_{\rm X}$) were calculated by multiplying the count rate by the energy conversion factor (ECF) provided in Fleming et al. (1995):

$$\mathrm{ECF} = (8.31 + 5.30\,\mathrm{HR1}) \times 10^{-12}\ \mathrm{erg\,cm^{-2}\,cr^{-1}}, \quad (4)$$

where cr^{-1} is the number of counts per second. Bolometric magnitudes were found using V magnitudes and a main-sequence bolometric correction interpolated from $V - K_s$ using table 5 in Pecaut & Mamajek (2013). Main-sequence conversions should be appropriate for the F, G and K stars in this sample, however, if stars were younger than 30 Myr this may result in a small calibration error of ∼0.1 dex.

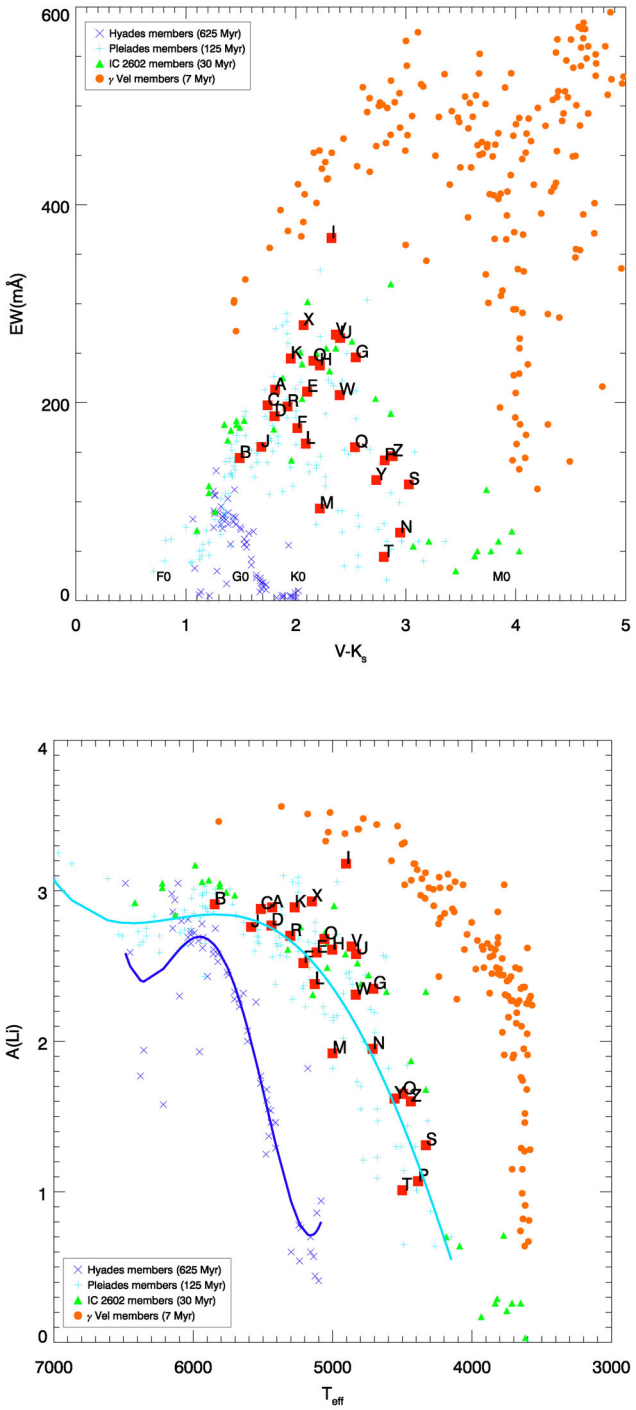

Figure 3. Top: Li EWs and corresponding $V - K_s$ colours. Green open circles and filled diamonds represent the same objects described in Fig. 1. Objects are compared to members in the Hyades (625 Myr), the Pleiades (125 Myr), IC 2602 (30 Myr) and γ Vel (10 Myr, see text for references) to estimate an Li-based age range. Error bars are not included, but are provided in Table 4. Bottom: Li abundances as a function of surface temperature. Both the target sample and all ancillary data from the open clusters are folded through the same curve of growth (described in Section 4.4). Fourth-order polynomial fits are overplotted for the Hyades and Pleiades, however these are not implied to represent the trend of Li abundances in these clusters. We display only the objects from Table 1 in the bottom panel and Li abundances for all other objects are provided in the online supplementary data.

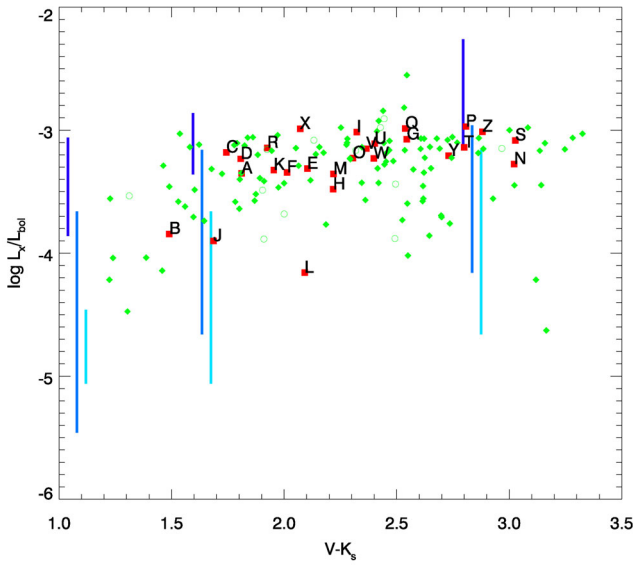

Figure 4. $\log L_X/L_{bol}$ as a function of $V - K_s$. The 10th to 90th percentile range of L_X/L_{bol} values in NGC 2547, the Pleiades and the Hyades are represented by the light blue/blue/dark blue lines, respectively.

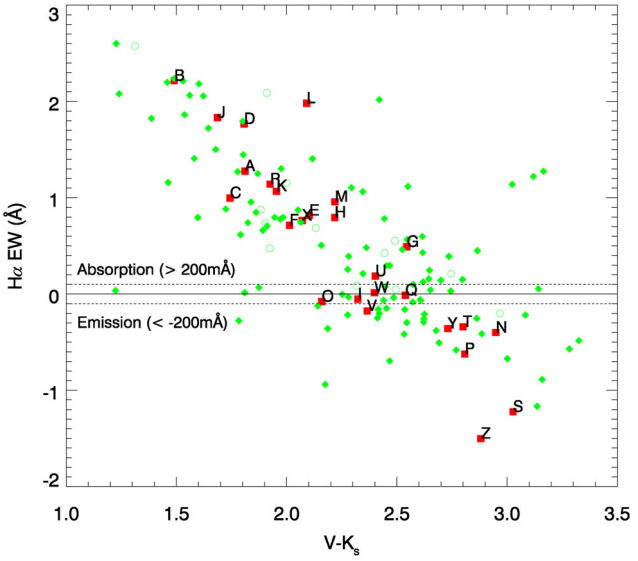

Figure 5. H α EW as a function of $V - K_s$. Objects displaying emission may be compared to an upper age limit based on chromospheric activity and a lower age limit for H α absorption. Only objects with EWs $>$ 200 mÅ ($<-$ 200 mÅ) were identified as true emission (or absorption) lines.

Fig. 4 shows L_X/L_{bol} as a function of $V - K_s$. For reference, the 10th and 90th percentile L_X/L_{bol} range for F, G and K stars in NGC 2547, the Pleiades and the Hyades (based on fig. 12 in Jeffries et al. 2006) are represented by light blue/blue/dark blue lines, (respectively). L_X/L_{bol} is a relatively crude age indicator and largely rotation-dependent in any case. Almost all of the candidates could be consistent with a Pleiades age (as expected for their rotation rates). As it turned out the probable young objects were slightly more active than the average star in our spectroscopic sample.

5.4 H α emission

A potentially more direct activity-age-dependent probe is to observe the strength of the H α line at 6563 Å. H α emission lines are diagnostic of strong magnetic activity in the photospheres of stars, which are linked to rotation and young ages.

The empirical behaviour is that young stars show H α emission, but this emission is not apparent in stars with photospheres warmer than a temperature that appears to be age-dependent (Reid, Hawley & Mateo 1995; Hawley et al. 1999). Using data from clusters ranging from 30–625 Myr (IC 2602, IC 2391, NGC 2516, Pleiades and Hyades) Hawley et al. (1999) derived a log-linear fit to the age (in Myr) of a cluster and the $V - I$ colour at which stars first display H α emission given as

$$(V - I)_{\rm emission} = -6.42 + 0.99(\log {\rm age/Myr}). \quad (5)$$

At redder colours there is a point where no stars have H α in absorption. Compiling data in seven open clusters aged between 30 and 625 Myr (NGC 2391 and NGC 2602, Stauffer et al. 1997; NGC 2547, Jeffries, Totten & James 2000; Blanco 1, Panagi & O'Dell 1997; Pleiades, Soderblom et al. 1993a; NGC 2516, Hawley et al. 1999; Hyades, Stauffer et al. 1991), we derived a relationship for a given $V - I$ and age at which a star has reduced in magnetic activity and starts to show H α in absorption:

$$(V - I)_{\rm absorption} = -4.19 + 0.68(\log {\rm age/Myr}). \quad (6)$$

These relationships can be used to estimate the minimum/maximum age of a star with an H α absorption/emission line. Targets with H α EW $>$ 200 mÅ are considered as emission lines (providing a maximum age) and EW < -200 mÅ for H α in absorption (a minimum age). Targets with H α EWs in the range $\pm$ 200 mÅ were considered as 'filled-in' lines and equations (5) and (6) were used to provide a likely age *range*. In Table 4, the H α EWs for the likely-young sample are presented, and the ages estimated for the entire sample are provided in Table 5. $V - I_C$ colours are converted to $V - K_s$ using table 5 in Pecaut & Mamajek (2013). The H α EWs of the entire observed sample are plotted as a function of their $V - K_s$ baseline in Fig. 5.

5.5 Radii–colour isochrones

We calculated projected rotational velocities ($v \sin i$) following the procedures in Section 4.3 and multiplied them by their rotational periods to obtain measurements of the projected stellar radius $R \sin i = 0.02\,Pv \sin i$ (in solar radii). Because of the $\sin i$ ambiguity, this technique is only capable of providing lower limits to the radius. Values of $R \sin i$ are compared to radius/$V - K_s$ isochrones from the models of Siess, Dufour & Forestini (2000). Between ages of 10–100 Myr a star is contracting on the PMS, and because the radii calculated from $R \sin i$ are minima, this sets an upper limit to the age. The $R \sin i$ values used correspond to the 1σ lower limit based on both the period and $v \sin i$ measurement, which sets a likely upper age limit. $R \sin i$ offers good age discrimination when dR/dt is large, but becomes poor when $dR/dt \sim 0$ as objects approach the ZAMS. The targets that displayed no Li yet appear to have large $R \sin i$ values are more likely to be binaries as opposed to being genuinely young. One object in Fig. 6, target M, has an $R \sin i$ age (5–10 Myr) in contradiction with the Li age (30–200 Myr) and is at odds with an H α lower limit of 32 Myr.

5.6 Combined age estimation and identification of young, single stars

In terms of providing a secure identification of youth, we regard *Li as the primary age indicator*. Alternative age indicators are used

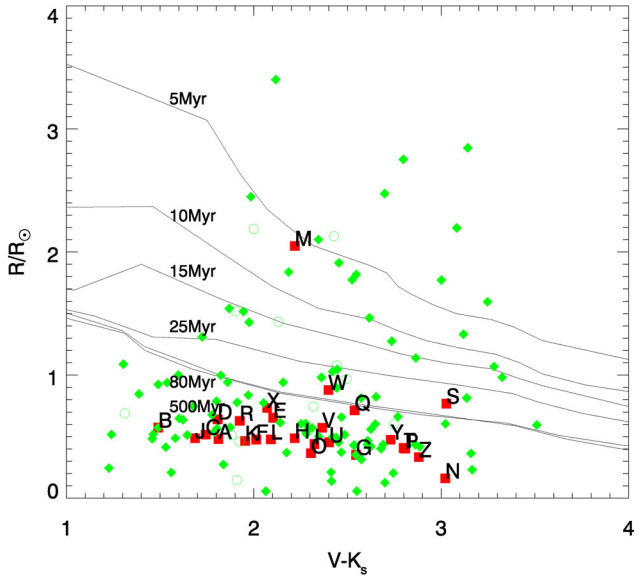

Figure 6. Radii–colour relationship for the entire observed sample (minus the six objects with an indeterminate $v \sin i$ measurement). Continuous lines represent isochrones generated from the models in Siess et al. (2000). The plotted points are $R \sin i$ values and therefore lower limits to the true radius.

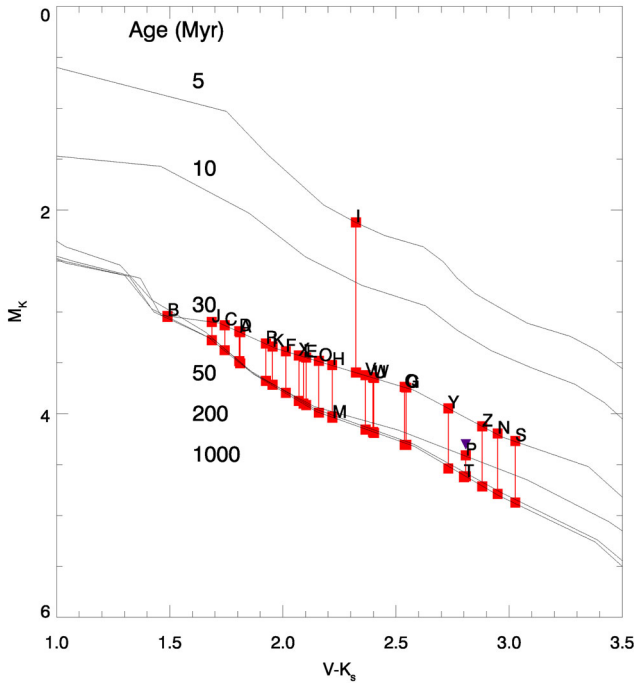

Figure 7. M_K versus $V - K_s$ CMD for the entire observed sample. Red lines indicate the range in M_K for the likely-young sample based on the assumed age range for each object. The model isochrones of Siess et al. (2000) are overplotted at 5, 10, 30, 200 and 1000 Myr. The purple downward-facing triangle is the absolute K magnitude for target P, measured from a trigonometric parallax.

only to support an age determination. If no Li is present in the spectra, then the object is automatically assumed to be at least older than the Hyades and is assigned a nominal age of 1 Gyr (for the purpose of a parallax estimation – see Section 6.1).

Subsequent analysis in this paper is restricted to 26 objects that have Li-derived ages younger than 200 Myr and have binary scores of 1 or 2. We categorize these objects as the *likely-young sample*. Table 5 shows that, with the exception of target I, all of the likely-young sample have Li-based ages which overlap with the ages constrained from H α. Each age estimate for the likely-young sample is provided in Table 5 (all other objects are listed online). $R \sin i$ values are only identified as younger than main sequence for three objects, two of which (targets S and W) are consistent with Li and H α and the other, target M, is discussed in Section 5.5. Target I has an age range of 5–30 Myr, significantly younger than the rest of the sample.

6 KINEMATIC ANALYSIS

6.1 Parallax estimation

Only four objects from the entire observed sample have a previously measured trigonometric parallax, only one of which is part of the likely-young sample. For the rest of the objects, parallaxes were estimated using $V - K_s$ (assuming no reddening) and a maximum and minimum age (see Table 5). Using the Siess et al. (2000) evolutionary models (with solar metallicity and no convective overshoot) a maximum and minimum absolute K magnitude was calculated by interpolating M_K for the youngest and oldest isochrone corresponding to the estimated age range, from which a 'photometric' parallax was calculated.

In Fig. 7 the M_K range is plotted for the likely-young sample, along with all other objects and TLSPBs. The plot shows that the younger objects span a larger range in M_K due to PMS contraction. For example, target I, with an age range from 5 to 30 Myr has a possible M_K range of ∼1.5 mag, whereas target V, with an age ranging between 30 and 70 Myr results in a difference in M_K of ∼0.5 mag. Redwards of $V - K_s = 3.0$ isochrones are separated by no more than 0.7 mag between 30 Myr and the ZAMS and no more than 0.3 mag between 50 Myr and the ZAMS.

To test the precision of the photometric parallaxes, absolute K magnitudes for the four objects with trigonometric parallaxes were estimated in the same way; one of which, target P, is a member of the likely-young sample, and is plotted as a purple downwards-pointing triangle. For each measurement the photometric parallax appears to underpredict the trigonometric parallaxes. The average difference between the M_K measured from trigonometric parallax and estimated M_K is ∼0.4 mag and the average range in M_K from photometric parallaxes is 0.44 mag. The parallax range for all objects is provided in column 6 of Table 6.

6.2 Calculating Galactic space velocities

Using the prescription in Johnson & Soderblom (1987), Galactic space velocities (and their errors) were computed in terms of U, V and W (where U points towards the Galactic Centre, V in the direction of Galactic rotation and W in the direction of the Galactic North Pole). The photometric parallax range is used if no trigonometric parallax is available. Table 6 lists all of the required input parameters and columns 5, 6 and 7 are the calculated UVW. Proper motions are from the PPMXL catalogue (Roeser et al. 2010). Two separate error bars are quoted, the first includes contributions from the σ_{μ_α}, σ_{μ_δ} and $\sigma_{\rm RV}$ uncertainties and the second corresponds to half of the range in each velocity coordinate resulting from the extrema of the possible photometric parallaxes (provided in column 6). Should a trigonometric parallax exist, or if an object is assigned a single-valued main-sequence age (1 Gyr) then all errors are incorporated into one single error bar.

Table 6. Kinematic data for the likely-young sample.

Target	μ_α (mas yr^{-1})	μ_δ (mas yr^{-1})	π (mas)	U (km s^{-1})	V (km s^{-1})	W (km s^{-1})	$v \sin i$ (km s^{-1})
A	11.9 ± 1.6	−14.0 ± 1.7	7.22–8.31	−7.4 ± 0.9 ± 0.2	−4.6 ± 0.9 ± 0.6	−10.2 ± 0.9 ± 0.4	8.0 ± 1.1
B[a]	12.2 ± 1.5	−0.6 ± 1.5	5.60–5.62	−10.6 ± 1.5	−3.9 ± 1.5	−1.9 ± 1.6	35.5 ± 0.5
C	38.9 ± 1.4	−21.9 ± 1.4	8.08–9.04	−12.9 ± 1.9 ± 0.7	−21.1 ± 1.3 ± 1.2	−1.5 ± 1.3 ± 0.1	20.5 ± 1.1
D	11.9 ± 1.7	−4.2 ± 1.7	6.67–7.64	−12.3 ± 2.1 ± 0.3	−3.2 ± 1.4 ± 0.5	−2.4 ± 1.4 ± 0.1	18.0 ± 0.5
E[b]	27.5 ± 2.1	−35.1 ± 2.1	9.48–11.75	−10.0 ± 0.7 ± 1.2	−16.2 ± 0.8 ± 1.6	−6.9 ± 1.0 ± 0.7	8.6 ± 0.5
F	12.4 ± 1.6	−14.6 ± 1.7	8.82–10.65	−10.2 ± 1.6 ± 0.2	−5.8 ± 1.0 ± 0.8	−5.5 ± 1.0 ± 0.2	14.6 ± 0.6
G[c]	22.5 ± 2.1	−46.2 ± 2.1	8.78–11.37	−6.6 ± 0.6 ± 0.2	−21.9 ± 1.0 ± 3.0	−10.9 ± 0.9 ± 1.1	6.2 ± 0.5
H	27.2 ± 1.3	−52.5 ± 1.3	9.76–12.34	−13.7 ± 0.6 ± 0.3	−23.8 ± 0.6 ± 2.9	−5.6 ± 0.6 ± 0.5	5.4 ± 0.2
I[d]	10.0 ± 1.2	−48.0 ± 1.2	6.46–12.74	−11.5 ± 0.5 ± 0.6	−25.4 ± 0.7 ± 8.2	−11.9 ± 0.7 ± 3.3	6.5 ± 0.4
J	−17.1 ± 2.2	−50.6 ± 2.1	7.87–8.55	−12.5 ± 0.9 ± 0.2	−29.5 ± 1.2 ± 1.2	−5.3 ± 1.1 ± 0.5	5.8 ± 1.2
K	−16.9 ± 1.6	7.4 ± 1.6	7.06–8.39	−10.7 ± 1.0 ± 0.9	−5.2 ± 1.0 ± 0.3	−5.5 ± 0.7	5.4 ± 0.5
L	−115.3 ± 1.4	−69.2 ± 1.5	18.20–22.50	−15.1 ± 0.4 ± 1.4	−27.6 ± 0.4 ± 3.0	−5.5 ± 0.5 ± 0.2	4.3 ± 1.2
M	−35.7 ± 1.9	−17.5 ± 1.9	11.02–11.08	−8.9 ± 0.8	−21.4 ± 0.8	−11.0 ± 0.6	20.4 ± 1.3
N	39.4 ± 1.6	−37.7 ± 1.6	25.25–33.18	−25.0 ± 0.4 ± 1.0	−37.2 ± 0.4 ± 0.1	−52.6 ± 0.5 ± 0.7	8.1 ± 0.9
O	16.6 ± 1.7	−7.5 ± 1.7	7.45–9.42	−8.3 ± 1.0 ± 0.5	−23.7 ± 1.5 ± 0.3	−1.3 ± 1.1 ± 1.0	14.6 ± 0.5
P[e]	−135.0 ± 1.1	55.2 ± 1.1	21.71 ± 1.64	−20.2 ± 0.2 ± 0.9	−5.4 ± 0.2 ± 0.2	−1.4 ± 0.7 ± 0.2	19.6 ± 0.4
Q	−62.8 ± 1.2	−72.5 ± 1.2	17.57–22.84	−6.9 ± 0.3 ± 0.2	−23.7 ± 0.3 ± 3.0	−5.5 ± 0.3 ± 0.1	16.2 ± 0.5
R	28.2 ± 1.4	−12.4 ± 1.4	8.25–9.76	−3.0 ± 0.7 ± 0.8	−8.1 ± 0.7 ± 0.5	−28.8 ± 0.8 ± 1.0	22.3 ± 0.4
S	−4.0 ± 1.7	76.3 ± 1.6	21.69–28.66	−32.1 ± 0.3 ± 1.7	−14.7 ± 0.3 ± 1.0	−13.4 ± 0.3 ± 0.6	16.1 ± 0.5
T	−37.3 ± 2.5	63.4 ± 2.4	24.10–24.19	−22.2 ± 0.5	−18.0 ± 0.5	−5.7 ± 0.5	16.8 ± 0.5
U	5.0 ± 1.5	63.2 ± 1.7	14.71–18.86	−25.0 ± 0.5 ± 1.9	−3.1 ± 0.5 ± 1.2	−5.4 ± 0.5 ± 0.4	18.3 ± 0.5
V	−22.4 ± 3.1	4.1 ± 3.1	7.78–9.95	−10.8 ± 1.6 ± 0.1	−0.6 ± 1.1 ± 27.0	−0.2 ± 1.6 ± 1.4	18.8 ± 0.5
W	30.9 ± 1.5	7.1 ± 1.5	16.61–21.26	−12.1 ± 0.4 ± 0.6	−29.2 ± 0.5 ± 0.3	−13.8 ± 0.4 ± 0.8	37.0 ± 0.4
X	18.9 ± 1.5	−7.0 ± 1.5	7.31–8.98	−7.5 ± 0.7 ± 0.6	−4.5 ± 0.8 ± 0.3	−8.5 ± 0.8 ± 1.0	16.5 ± 0.5
Y	38.1 ± 1.3	16.2 ± 1.3	11.31–14.84	−15.1 ± 0.5 ± 2.0	−3.3 ± 0.5 ± 0.2	−0.4 ± 0.5 ± 0.2	21.9 ± 0.4
Z	105.7 ± 2.0	−85.7 ± 1.4	17.58–23.06	−11.4 ± 0.5 ± 1.5	−25.6 ± 0.3 ± 2.6	−18.1 ± 0.4 ± 3.2	15.8 ± 0.5

[a] $v \sin i = 34.0$ km s^{-1} (Glebocki & Gnacinski 2005), [b] Likely α Persei member (Hoogerwerf & Blaauw 2000), [c] Pleiades member (Sarro et al. 2014), $v \sin i = 11.0 \pm 3.00$ km s^{-1} (Glebocki & Gnacinski 2005), $v \sin i = 12.2 \pm 1.0$ km s^{-1} (Mermilliod et al. 2009), [d] $v \sin i = 15.6 \pm 1.0$ km s^{-1} (Biazzo et al. 2012). [e] Parallax from de Bruijne & Eilers 2012.

In Fig. 8, the likely-young sample are plotted on Boettlinger $U - V$ and $V - W$ diagrams. Their space motions are compared with 10 nearby MGs (the *UVW* used to define 1σ errors for the MGs are taken from table 1 in Gagné et al. 2014 and are listed in Table 7). With the exception of target P, which has a measured parallax, velocity error bars on this plot do not include an error due to the parallax uncertainty. Instead, a line connects *UVW* points calculated at the extrema of the distances inferred from the photometric parallaxes. The object plotted in blue is target I which had an age range significantly younger than the rest of the sample (see Table 5). We also note that our analysis does not consider the possibility that our targets could be unresolved binaries which would enlarge our parallax errors.

6.3 Comparison with MG space velocities

To test if a star is kinematically matched in *UVW* to a known MG, a reduced χ^2 fitting statistic is used, as described in Shkolnik et al. (2012):

$$\bar{\chi}^2_{\rm T} = \frac{1}{3}\left(\frac{(U_* - U_{\rm MG})^2}{\sigma^2_{U_*} + \sigma^2_{U_{\rm MG}}} + \frac{(V_* - V_{\rm MG})^2}{\sigma^2_{V_*} + \sigma^2_{V_{\rm MG}}} + \frac{(W_* - W_{\rm MG})^2}{\sigma^2_{W_*} + \sigma^2_{W_{\rm MG}}}\right). \quad (7)$$

With the exception of target P, the *UVW* mid-point values are used as inputs for *UVW* and half the line length is used for the errors. Table 8 provides the reduced $\bar{\chi}^2_{\rm T}$ values for all of the likely-young sample. To interpret these results, given there are 3 degrees of freedom, a $\bar{\chi}^2_{\rm T}$ value larger than 3.78 rejects the null hypothesis at 99 per cent confidence. Any candidate/MG test where $\bar{\chi}^2_{\rm T} > 3.78$ results in rejection for membership of that MG.

6.4 Predicted RV comparisons with known MGs

The Boettlinger diagrams require distances, which, with one exception for the likely-young sample, could only be inferred using photometric parallaxes. Therefore a *distance-independent* criterion was used to strengthen the case for MG membership. We have recalculated the convergent points of each MG using the membership lists provided by Gagné et al. (2014), Zuckerman et al. 2013 (for Octans-Near) and Murphy et al. 2013 (for ϵ and η Cha). Given the *UVW* and convergent point of an MG and the position of a candidate member, the predicted RV for a group member is then $V_{\rm T} \cos\lambda$, where $V_{\rm T}$ is the total velocity of the group ($\sqrt{U^2 + V^2 + W^2}$) and λ is the angle between the convergent point and the target position.

The average RV error for the likely-young sample is $\sim$1 km s^{-1} and the dispersion amongst MG members in *UVW* is $\lesssim$3 km s^{-1}. Therefore true MG members are required to have RVs that are within 5 km s^{-1} of the predicted RV (ΔRV $= |{\rm RV} - V_{\rm T} \cos\lambda| < 5$ km s^{-1}). Any candidates with ΔRV > 5 km s^{-1} are rejected as MG members. Objects that have RVs within this threshold are flagged as possible members, although even if they satisfy this criterion, a discrepancy in distance, age or chemical abundances may result in a rejection. For this reason the technique can only be used to eliminate membership. The convergent point of each MG (following the prescription in Jones 1971) is given in Table 7 and values of ΔRV for each candidate/MG are given in Table 9.

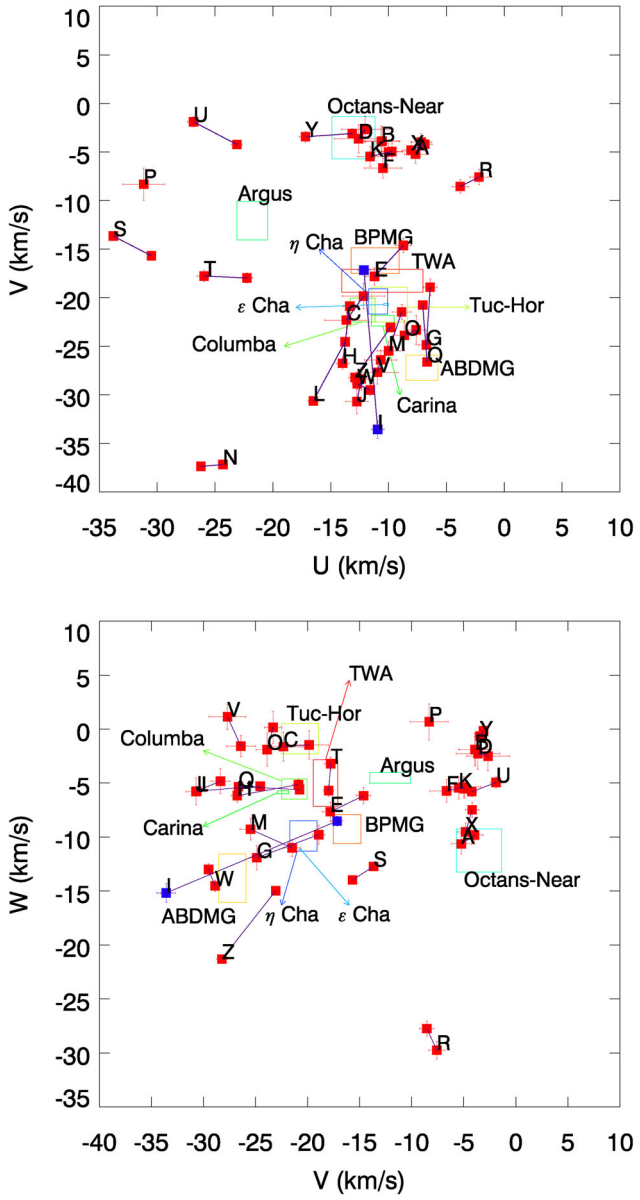

Figure 8. Boettlinger diagrams in $U - V$ and $V - W$ space highlighting the space motions of the characteristically young, likely-single objects in this paper. Each object is connected by a solid purple line which indicates distance uncertainties due to the photometric parallax method described in Section 6.1. Labels for the likely-young sample are the same as in Table 1.

In Section 4.6, it was calculated that there is a 7.2 per cent chance that a star has 2 RV measurements within 5 km s^{-1} but is still >5 km s^{-1} from the average centre-of-mass RV. This implies that out of a sample of 26 Li-rich stars likely to be single based on repeat RV measurements, ∼2 may be shifted in *UVW* by ∼5 km s^{-1} which would potentially alter our assessment of their membership status for any MG.

In principle, we could perform a similar test using the tangential velocities, if the distance and proper motion are known accurately (i.e. $\delta V_{\rm TAN} < 5$ km s^{-1}). In practice, we can only do this on the one object – target P, which is within 4.6 km s^{-1} of ABDMG but >5 km s^{-1} for all other MGs.

6.5 Combined MG membership criteria

In this work, a candidate only remains a possible member of an MG if it satisfies all of the following criteria.

(i) The $\bar{\chi}^2_T$ value in Table 8 is no more than 3.78.
(ii) ΔRV values in Table 9 are no more than 5 km s^{-1}.
(iii) The estimated age range for the candidates (provided in Table 5) must overlap with the age range of the MG, which are provided in a supplementary online table.

In Table 10 the outcome for each criteria is given. A ✔ indicates a successful criterion match and an ✖ represents a failure.

6.6 Comparison with BANYAN

Malo et al. (2013) and Gagné et al. (2014) have presented tools for the Bayesian Analysis of Nearby Young AssociatioNs (BANYAN I and BANYAN II, respectively). These tools attempt to assign each star a probability of membership for seven well-defined MGs (TWA, BPMG, Tuc-Hor, Columba, Carina, Argus, ABDMG) using sky position, proper motion, photometry and, where available, radial velocities and parallaxes, as inputs. BANYAN II is an improvement over BANYAN I in terms of its treatment of uncertainties and a more realistic assessment of the likely field star contamination using the Besançon Galactic model (Robin et al. 2012).

We have used the provided web-based tools[3] to test MG membership for our sample of 26 likely young objects. Using the BANYAN I technique, almost all our targets have zero or very low probability of membership for any of the tested MGs. In BANYAN II, the more realistic incorporation of the field population results in even lower probabilities; none of our young targets has an MG membership probability of more than 2 per cent.

The results from BANYAN appear to contradict the assessments we have made in Section 6.5. The reason appears to be a philosophical difference in how MG membership is defined. BANYAN requires that new MG members have similar spatial coordinates to those members that are already known. The predominantly Northern hemisphere locations of our targets mean that their *XYZ* positions are far from the centres of most of the MGs (as defined in BANYAN). Consequently, the membership probabilities are very low. However, in this paper we choose to define members of MGs only on the basis of their youth and kinematics and so do not consider the BANYAN membership probabilities any further.

7 INDIVIDUAL OBJECTS

7.1 Individual objects linked to at least one MG

Here, we focus on objects that satisfied all three criteria in Section 6.5 for at least one MG. The following section discusses any of these objects that have literature sources pertaining to MG membership and we compare them to our findings in this work.

Target G – All three criteria are successfully matched with ABDMG. Although target G satisfies both the $\bar{\chi}^2_T$ and RV criteria, we have not assigned it to BPMG because its age is measured between 30 and 150 Myr, too old to be a BPMG member (21–26 Myr, see Table 7). The age of this object is more likely to be coeval with ABDMG (between 70 and 125 Myr). There is an uncertainty of ∼4 km s^{-1} in *V* velocity, which means the object could have kinematic matches to Tuc-Hor or TWA (but not BPMG). A literature

[3] Available at http://www.astro.umontreal.ca/∼malo/banyan.

Table 7. Properties of the nearest known MGs within 100 pc. Column 2 is the number of MG objects with a measured parallax, from Gagné et al. (2014). The age ranges used for each MG are from the following publications: TWA, Columba, Carina, Argus and ABDMG (Gagné et al. 2014); Octans-Near (Zuckerman et al. 2013); η Cha (Luhman 2004) and ϵ Cha (Murphy, Lawson & Bessell 2013). The age ranges for BPMG (Binks & Jeffries 2014; Malo et al. 2014b) and Tucana-Horologium (Tuc-Hor, Kraus et al. 2014) are solely from the 'lithium depletion boundary' technique. *UVWXYZ* are from Gagné et al. (2014), except for Octans (calculated from the available data in Zuckerman et al. 2013) and η and ϵ Cha (Murphy et al. 2013). Columns 7 and 8 correspond to the convergent points in right ascension and declination, respectively.

Name	N	Age (Myr)	Distance (pc)	*UVW* σ_{UVW} (km s^{-1})	*XYZ* σ_{XYZ} (pc)	α_{CP} (°)	δ_{CP} (°)
TWA	12	8–12	42–92	−10.53, −18.27, −5.00	12.17, −43.23, 21.90	180.87	−79.93
				3.50, 1.17, 2.15	6.14, 7.30, 3.06		
BPMG	44	21–26	9–73	−11.16, −16.19, −9.27	4.35, −5.82, −13.29	88.00	−30.16
				2.06, 1.32, 1.35	31.43, 15.04, 7.56		
ABDMG	48	70–120	11–64	−7.11, −27.21, −13.82	−2.25, 2.93, −15.42	92.89	−47.73
				1.39, 1.31, 2.26	20.10, 18.97, 15.37		
Tuc–Hor	42	39–43	36–71	−9.93, −20.72, −0.89	11.80, −20.79, −35.68	116.28	−28.80
				1.55, 1.79, 1.41	18.57, 9.14,5.29		
Columba	20	20–40	35–81	−12.24, −21.27, −5.56	−28.22, −29.74, −28.07	103.27	−29.79
				1.08, 1.22, 0.94	13.68, 23.70, 16.09		
Carina	5	20–40	46–88	−10.50, −22.36, −5.84	15.55, −58.53, −22.95	104.93	−34.25
				0.99, 0.55, 0.14	5.66, 16.69, 2.74		
Argus	11	30–50	8–68	−21.78, −12.08, −4.52	14.60, −24.67, −6.72	91.93	−1.24
				1.32, 1.97, 0.50	18.60, 19.06, 11.43		
Octans-Near	14	30–100	24–98	−13.04, −3.53, −11.24	8.07, 25.32, −48.97	60.12	−4.74
				1.86, 2.17, 2.00	3.76, 11.81, 22.83		
η Cha	4	5–10	∼97	−10.20, −20.70, −11.20	33.40, −81.00, −34.90	89.86	−37.55
				0.20, 0.10, 0.10	0.40, 1.00, 0.40		
ϵ Cha	35	3–5	100–120	−10.90, −20.40, −9.90	54.00, −92.00, −26.00	92.48	−35.13
				0.80, 1.30, 1.40	3.00, 6.00, 7.00		

Table 8. $\bar{\chi}^2_T$ values for each candidate/MG match in the likely-young sample.

Target	TWA	BPMG	ABDMG	Tuc-Hor	Columba	Carina	Argus	Octans-Near	η Cha	ϵ Cha
A	45.9	22.2	81.5	38.3	62.3	186.8	68.2	3.2	240.5	45.7
B	63.1	38.8	116.9	29.6	73.4	638.7	38.8	7.9	11 511.3	64.6
C	16.1	13.5	18.2	1.1	6.1	230.8	27.9	24.3	1808.2	13.0
D	62.1	37.3	111.8	31.0	67.2	346.4	28.5	6.6	1490.7	61.9
E	10.8	0.9	13.0	5.9	3.2	5.1	17.4	9.4	13.4	2.7
F	36.8	17.3	69.4	22.6	37.6	92.4	28.7	3.7	346.5	33.1
G	10.4	3.0	1.4	12.2	13.6	12.4	55.8	12.3	65.6	9.6
H	16.9	4.4	11.6	5.5	0.8	3.2	16.5	12.8	67.7	6.5
I	14.1	0.6	3.0	3.5	1.3	1.4	19.1	2.4	1.6	0.3
J	29.9	21.8	10.1	9.5	8.0	12.1	35.8	39.9	91.3	13.7
K	50.9	24.8	96.3	28.1	55.5	264.8	20.9	3.4	1901.8	47.0
L	18.3	7.3	10.1	6.9	2.2	3.9	11.3	16.8	176.9	7.1
M	13.9	3.4	2.4	10.8	6.4	8.4	40.8	16.4	1.7	1.3
N	265.1	361.1	146.2	403.5	602.5	1599.4	1039.7	216.4	5716.4	342.3
O	16.8	18.9	11.6	1.2	8.9	10.5	45.6	37.3	69.7	13.8
P	44.8	29.2	83.5	24.1	47.5	132.2	10.4	10.8	245.2	47.4
Q	9.2	5.9	4.9	5.0	8.2	5.6	46.5	16.6	436.3	11.7
R	59.8	60.5	77.1	107.4	144.6	310.8	206.9	30.0	347.7	82.5
S	47.0	23.9	64.0	56.8	55.7	103.5	49.4	27.2	73.6	50.4
T	25.5	10.1	39.1	13.5	12.9	35.8	3.2	23.2	161.6	18.3
U	54.9	29.2	87.1	38.6	50.3	90.2	6.4	9.6	153.7	51.9
V	28.0	25.7	11.2	3.8	9.9	16.0	43.0	43.4	55.8	15.2
W	45.7	33.5	4.5	29.4	28.6	74.6	74.1	46.2	227.6	16.9
X	52.4	25.8	96.3	33.7	65.7	271.0	41.8	3.3	832.5	51.4
Y	68.8	46.0	124.9	32.9	81.3	495.3	27.3	9.8	3401.3	73.2
Z	17.1	5.8	1.9	9.2	5.7	5.6	20.6	15.6	3.0	3.0

Table 9. ΔRV values for all MG/candidate comparisons.

Target	TWA	BPMG	ABDMG	Tuc-Hor	Columba	Carina	Argus	Octans-Near	η Cha	ϵ Cha
A	21.0	5.5	11.5	13.8	10.1	11.5	0.1	4.3	7.5	7.7
B	17.2	1.4	6.4	9.8	5.8	7.2	3.6	7.6	3.0	3.3
C	14.8	4.5	1.9	2.4	1.2	0.5	12.4	12.8	2.4	2.5
D	23.6	3.2	9.0	9.5	5.9	7.6	5.1	4.1	5.0	4.8
E	17.4	1.0	8.9	2.9	1.3	3.4	11.8	10.3	2.5	1.8
F	22.1	1.2	6.6	7.1	3.5	5.2	7.4	5.4	2.8	2.6
G	16.8	4.5	0.7	1.1	2.9	1.2	12.7	9.6	3.6	3.7
H	23.2	1.1	6.0	3.8	1.1	2.9	9.3	2.5	2.4	1.8
I	22.9	0.9	4.1	3.1	0.2	1.8	9.0	0.9	1.5	1.0
J	19.2	5.2	9.8	0.4	1.4	2.8	5.5	6.5	6.6	5.2
K	5.0	7.2	15.4	0.9	5.4	6.1	0.8	4.7	10.6	9.2
L	10.9	4.3	2.7	4.4	0.4	0.6	7.2	10.6	4.1	3.4
M	11.2	2.8	4.0	9.2	4.2	4.1	5.9	4.7	0.2	0.9
N	59.9	47.9	40.6	51.8	47.2	47.2	48.5	52.7	44.6	45.3
O	9.5	9.1	1.2	2.4	3.1	2.4	9.6	21.3	5.8	5.5
P	1.6	6.4	10.5	1.9	3.1	3.1	3.5	8.4	8.3	7.1
Q	14.4	5.1	5.6	0.6	4.1	3.0	10.2	6.8	5.9	5.6
R	17.1	4.5	2.6	8.3	3.7	3.8	4.6	9.2	1.2	1.9
S	26.8	13.3	6.4	15.5	11.4	11.6	12.2	19.2	10.1	10.5
T	13.4	3.9	5.1	5.6	1.7	1.4	5.2	11.3	0.1	0.5
U	8.9	3.4	11.0	1.8	5.7	5.7	4.1	3.3	7.0	6.5
V	13.0	5.0	4.6	5.3	1.9	1.6	6.5	13.9	0.8	1.3
W	17.5	13.6	3.0	11.5	9.4	8.7	16.1	24.7	9.1	9.5
X	2.5	8.3	9.1	14.4	13.7	13.0	15.5	1.7	9.1	10.1
Y	9.7	5.6	12.1	14.1	11.9	12.7	5.0	5.9	8.2	8.7
Z	2.7	1.7	4.0	7.1	4.5	5.2	2.0	12.8	0.6	1.1

Table 10. The full list of candidate/MG criteria matches for the likely-young sample. A ✔ marks a successful match and a ✖ denotes a failed criteria. The columns labelled '1, 2 and 3' are the criteria listed in Section 6.5. An object was only considered a potential member of an MG if all three were satisfied.

	TWA			BPMG			ABDMG			Tuc-Hor			Columba			Carina			Argus			Octans-Near			η Cha			ϵ Cha		
Target	1	2	3	1	2	3	1	2	3	1	2	3	1	2	3	1	2	3	1	2	3	1	2	3	1	2	3	1	2	3
A	✖	✖	✖	✖	✖	✖	✖	✖	✔	✖	✖	✔	✖	✖	✔	✖	✖	✔	✖	✔	✔	✔	✔	✔	✖	✖	✖	✖	✖	✖
B	✖	✖	✖	✖	✔	✖	✖	✖	✔	✖	✖	✔	✖	✖	✔	✖	✖	✔	✖	✔	✔	✖	✖	✔	✖	✔	✖	✖	✔	✖
C	✖	✖	✖	✖	✔	✖	✖	✔	✔	✔	✔	✔	✖	✔	✔	✖	✔	✔	✖	✖	✔	✖	✖	✔	✖	✔	✖	✖	✔	✖
D	✖	✖	✖	✖	✔	✖	✖	✖	✔	✖	✖	✔	✖	✖	✔	✖	✖	✔	✖	✖	✔	✖	✔	✔	✖	✔	✖	✖	✔	✖
E	✖	✖	✖	✔	✔	✖	✖	✖	✔	✖	✔	✔	✔	✔	✔	✖	✔	✔	✖	✖	✔	✖	✖	✔	✖	✔	✖	✔	✔	✖
F	✖	✖	✖	✖	✔	✖	✖	✖	✔	✖	✖	✔	✖	✔	✔	✖	✖	✔	✖	✖	✔	✔	✖	✔	✖	✔	✖	✖	✔	✖
G	✖	✖	✖	✔	✔	✖	✔	✔	✔	✖	✔	✔	✖	✔	✔	✖	✔	✔	✖	✖	✔	✖	✖	✔	✖	✔	✖	✖	✔	✖
H	✖	✖	✖	✖	✔	✖	✖	✖	✔	✖	✔	✔	✔	✔	✔	✔	✔	✔	✖	✖	✔	✖	✔	✔	✖	✔	✖	✖	✔	✖
I	✖	✖	✔	✔	✔	✔	✔	✔	✖	✔	✔	✔	✔	✔	✔	✔	✔	✔	✖	✖	✔	✔	✔	✔	✔	✔	✔	✔	✔	✔
J	✖	✖	✖	✖	✖	✖	✖	✖	✔	✖	✔	✔	✖	✔	✔	✖	✔	✔	✖	✖	✔	✖	✖	✔	✖	✖	✖	✖	✖	✖
K	✖	✔	✖	✖	✖	✖	✖	✖	✔	✖	✔	✔	✖	✖	✔	✖	✖	✔	✖	✔	✔	✔	✔	✔	✖	✖	✖	✖	✖	✖
L	✖	✖	✖	✖	✔	✖	✖	✔	✔	✖	✔	✔	✔	✔	✔	✖	✔	✔	✖	✖	✔	✖	✖	✔	✖	✔	✖	✖	✔	✖
M	✖	✖	✖	✔	✔	✖	✔	✔	✔	✖	✖	✔	✖	✔	✔	✖	✔	✔	✖	✖	✔	✖	✔	✔	✔	✔	✖	✔	✔	✖
N	✖	✖	✖	✖	✖	✖	✖	✖	✔	✖	✖	✔	✖	✖	✔	✖	✖	✔	✖	✖	✔	✖	✖	✔	✖	✖	✖	✖	✖	✖
O	✖	✖	✖	✖	✖	✖	✖	✔	✔	✔	✔	✔	✖	✔	✔	✖	✔	✔	✖	✖	✔	✖	✖	✔	✖	✖	✖	✖	✖	✖
P	✖	✔	✖	✖	✖	✖	✖	✖	✔	✖	✔	✔	✖	✔	✔	✖	✔	✔	✖	✔	✔	✖	✖	✔	✖	✖	✖	✖	✖	✖
Q	✖	✖	✖	✖	✖	✖	✖	✖	✔	✖	✔	✔	✖	✔	✔	✖	✔	✔	✖	✖	✔	✖	✖	✔	✖	✖	✖	✖	✖	✖
R	✖	✖	✖	✖	✔	✖	✖	✔	✔	✖	✖	✔	✖	✔	✔	✖	✔	✔	✖	✔	✔	✖	✖	✔	✖	✔	✖	✖	✔	✖
S	✖	✖	✖	✖	✖	✖	✖	✖	✔	✖	✖	✔	✖	✖	✔	✖	✖	✔	✖	✖	✔	✖	✖	✔	✖	✖	✖	✖	✖	✖
T	✖	✖	✖	✖	✔	✖	✖	✖	✔	✖	✖	✔	✖	✔	✔	✖	✔	✔	✔	✖	✔	✖	✖	✔	✖	✔	✖	✖	✔	✖
U	✖	✖	✖	✖	✔	✖	✖	✖	✔	✖	✔	✔	✖	✖	✔	✖	✖	✔	✖	✔	✔	✖	✔	✔	✖	✖	✖	✖	✖	✖
V	✖	✖	✖	✖	✔	✖	✖	✔	✔	✔	✖	✔	✖	✔	✔	✖	✔	✔	✖	✖	✔	✖	✖	✔	✖	✔	✖	✖	✔	✖
W	✖	✖	✖	✖	✖	✖	✖	✔	✔	✖	✖	✔	✖	✖	✔	✖	✖	✔	✖	✖	✔	✖	✖	✔	✖	✖	✖	✖	✖	✖
X	✖	✔	✖	✖	✖	✖	✖	✖	✔	✖	✖	✔	✖	✖	✔	✖	✖	✔	✖	✖	✔	✔	✔	✔	✖	✖	✖	✖	✖	✖
Y	✖	✖	✖	✖	✖	✖	✖	✖	✔	✖	✖	✔	✖	✖	✔	✖	✖	✔	✖	✔	✔	✖	✖	✔	✖	✖	✖	✖	✖	✖
Z	✖	✔	✖	✖	✔	✖	✔	✔	✔	✖	✖	✔	✖	✔	✔	✖	✖	✔	✖	✔	✔	✖	✖	✔	✔	✔	✖	✔	✔	✖

search for this object using the SIMBAD[4] data base reveals that it was classified as a Pleiades member (Pels 22) by van Leeuwen, Alphenaar & Brand (1986) and has since been used as a Pleiades member in at least seven subsequent publications. Target G is very close to the centroid of the Pleiades cluster (α, δ = 03$^{\rm h}$47$^{\rm m}$00$^{\rm s}$, +24°07′00″) and it has an RV consistent to within 1σ, however the parallax range used in this work (8.78–11.37 mas) does not

[4] http://simbad.u-strasbg.fr/simbad/

encompass the Pleiades (7.34 ± 0.06 mas, Melis et al. 2014), which casts doubt on its membership. If target G were an equal mass binary, an increase of 0.75 mag (half the flux) may resolve the distance discrepancy.

Target I – Although this K3 spectral-type object matches all three criteria for seven MGs (BPMG, Tuc-Hor, Columba, Carina, Octans, η Cha and ϵ Cha), there is a large uncertainty in V velocity. Fig. 8 shows that membership with Tuc-Hor, Carina, Columba and Octans-Near cannot be ruled out, however a more accurate parallax is required to identify which group it may belong to. The object has an Li EW (>300 mÅ), large enough to set an age <30 Myr. Li & Hu (1998) identify this object as a weak-lined T-Tauri star (WTTS) in the surrounding area of the Taurus-Auriga region. It is classified as a T-Tauri star in the PMS catalogue developed by Ducourant et al. (2005), however no excess emission indicative of circumstellar material is observed at near-infrared wavelengths. The distance to Taurus (140 pc, ∼7.1 mas, Güdel 2007) is within our photometric parallax range of 6.46–12.74 mas.

Santos et al. (2008) located the object in the Taurus SFR and derive chemical abundances. To test for abundance matches with MGs, the mean and standard deviations of [Fe/H], [Si/H] and [Ni/H] for members of the MGs in tables 2 and 3 in Viana Almeida et al. (2009) were compared to target I. The abundances are consistent with any of the considered MGs to within 1σ uncertainties. Biazzo et al. (2012) identify this target as part of a 2–10 Myr stellar aggregate within 15° of Taurus-Auriga, which they name 'X-Clump 0534+22'.

Target Z – This target is matched with ABDMG and membership is rejected for TWA because target Z is too old to be coeval with TWA. The Li EW/$V - K_s$ of the target sets an age range of 30–150 Myr (see Fig. 3). Li, Hu & Chen (2000) identify the object as a possible WTTS and Ducourant et al. (2005) include it as a member in the PMS stars proper motion catalogue. The *UVW* values all lie outside the ABDMG box in Fig. 8, however, the *UVW* uncertainties from parallax estimation are large. A more precise age and parallax are necessary to test if it is an ABDMG member.

7.2 Individual objects not linked to any MG

Target B – At a spectral-type of G1 and Li EW of 154 mÅ this target is assigned an age range of 30–200 Myr, supported by a lower age limit of 20 Myr using H α measurements. In terms of *UVW* velocity, it appears consistent in $U - V$ with Octans-Near, however the W velocity of the target is $\sim$10 km s^{-1} larger than Octans-Near. Favata et al. (1995) measure a $v \sin i$ value of 34 km s^{-1} (no error bars provided), which is 1.5 km s^{-1}(3σ) slower than the measurement in this work.

Target D – The age measured for the target is 30–200 Myr based on Li measurements. This age is supported by a lower age limit of 20 Myr set by H α measurements. It is in the range of Octans-Near members in terms of U and V velocity, but is $\sim$10 km s^{-1} larger in W. It is flagged as a candidate WTTS in Taurus-Auriga region in Li & Hu (1998) and our photometric parallax range is consistent with this idea.

Target F – Age estimates are 30–200 Myr from Li measurements, and >25 Myr based on H α measurements. It appears consistent with the U and V velocities of Octans-Near, but is around 5 km s^{-1} larger in W.

Target J – An age range of 30–150 Myr was estimated from Li measurements, consistent with a lower age limit of 20 Myr set by H α. It is >5 km s^{-1} in U, V and W from any of the 10 MGs considered.

Target N – Although target N has an Li EW of 86 mÅ, because it is a late-K dwarf it is estimated to have an age of 30–150 Myr, with an upper limit of 189 Myr set by H α measurements. The W velocity is matched to a few MGs, however, both the U and V are at least $\sim$15 km s^{-1} from any MG.

Target P – Using Li, an age of 30–150 Myr was estimated and H α measurements suggest an age of 65–125 Myr. It has a U, V and W velocity at least 10 km s^{-1} from any MG. Xing & Xing 2012 include this target as a young K4V object (we calculate K5) with a Li EW of 17 mÅ which is almost 150 mÅ lower than the measurement in this work. It is listed as a possible visual binary in Makarov 2003, however, two consistent RV measurements in this analysis suggest the object is not a close binary.

Target Q – The age range of 30–150 Myr may be more consistent with the pattern observed in IC 2602 given the spectral-type K5 and Li EW of 174 mÅ. The H α age is estimated as 40–65 Myr. The U and V velocities are consistent with ABDMG, however its W velocity is too large by $\sim$10 km s^{-1}.

Target R – An age of 30–150 Myr constrained by Li measurements is supported by an age of >20 Myr from H α. It is at least 10 km s^{-1} from any MG in either U, V or W.

Target S – Because target S has a late-K spectral-type, its Li EW (135 mÅ) leads to an age of 30–150 Myr, supported by an H α age of <230 Myr and an $R \sin i$ age of <80 Myr. It is >5 km s^{-1} from any MG in U, V or W.

Target T – Its Li EW is only 62 mÅ, however, as it is a late-K type, it was estimated to have an age of 100–200 Myr. This is too old to be a BPMG member. An limit of <120 Myr is provided because H α is in emission. There are no matches <5 km s^{-1} in all *UVW* velocities for any MG.

Target U – This target has an age range of 30–150 Myr, however given the large Li EW (278 mÅ), this is more likely towards the younger end of this range. It has an H α age older than 35 Myr. There are no matches within 5 km s^{-1} for U, V or W for any MG and BPMG membership can be ruled out based on both the kinematics and age.

Target V – The age range is estimated as 30–150 Myr from Li and <50 Myr based on H α emission. Target V is not within 5 km s^{-1} in U, V or W for any MG.

Target W – This object satisfies the RV criteria in Section 6.4 for ABDMG (see Table 9) and its location in $U - V$ and $V - W$ velocity space suggests that it is similar to ABDMG in V and W but is more than 5 km s^{-1} from ABDMG in U velocity and therefore fails membership test 1, although only marginally ($\bar{\chi}^2_T = 4.5$, the membership criteria is $\bar{\chi}^2_T < 3.78$). The U, V and W are precise to within 1 km s^{-1} in each velocity coordinate. The Li EW measurement of 222 mÅ at an early-K spectral-type results in an age range of 30–150 Myr and although there is significant scatter amongst IC 2602 and Pleiades objects at this spectral-type, this target is more consistent with the lower envelope of IC 2602. The H α age range is 35–55 Myr and an age of <80 Myr is implied by $R \sin i$.

Frasca et al. (2011) identify differential rotation based on data from the *Kepler* mission. Their Li EW measurement is ∼50 mÅ larger

and their 1.0 Å H α EW is certainly not consistent with the 0.1 Å absorption line measured in this work. The $v \sin i$ measurements match to 1σ and their calculated inclination angle, i ($\simeq 70^{\circ}$), provides a stellar radius of $0.93\,R_{\odot}$, which from Fig. 6 suggests an age of 25–80 Myr, where the $\sin i$ ambiguity has been resolved. This is at least 40 Myr younger than ABDMG (if indeed ABDMG is coeval with the Pleiades), making membership for ABDMG unlikely. The authors also note that the object is flagged as an equal-magnitude visual binary system in the WDS Catalogue (WDS 19251+4431, Worley & Douglass 1997) and the Tycho Double Star Catalogue (Fabricius et al. 2002). Based on the orbital properties calculated by Frasca et al. (2011), if it were an equal-mass binary it would be expected to have RV variations $>5\,\mathrm{km\,s^{-1}}$ over 3–4 yr. The RVs reported by Frasca et al. (2011) were from three separate observations between 2007 and 2009 (-33.1, -33.1, $-32.2\,\mathrm{km\,s^{-1}}$) and the measurement of $-33.5 \pm 0.6\,\mathrm{km\,s^{-1}}$ in this work carried out in 2011 June suggests that the object is not in an equal-mass visual binary system.

Target Y – This target has a spectral-type K4 and a Li EW of 141 mÅ, from which an age range of 30–150 Myr was estimated, and an H α emission line implies an age of <100 Myr. It is within the range of Octans-Near in U and V velocity, but has a W velocity $\sim 5\,\mathrm{km\,s^{-1}}$ larger than Octans-Near.

7.3 Connection with the Octans-Near association?

In a *Hipparcos*-based survey, Zuckerman et al. (2013) report 14 star systems with spectral types between G5 and A0 and distances ranging from 24 to 98 pc that have ages between $\sim$30 and 100 Myr and Galactic space velocities similar to the mean space motion of Octans ($UVW_{\mathrm{Octans}} = -14.5 \pm 0.9, -3.6 \pm 1.6, -11.2 \pm 1.4\,\mathrm{km\,s^{-1}}$; $UVW_{\mathrm{sample}} = -13.0 \pm 1.9, -3.5 \pm 2.2, -11.2 \pm 2.0\,\mathrm{km\,s^{-1}}$). Torres et al. (2008) measure the distance of Octans to be 141 ± 34 pc and given that the 14 star systems in Zuckerman et al. (2013) are closer than the Octans association (all within 100 pc), the authors describe this stellar aggregate as the 'Octans-Near' group. More recently, Murphy et al. (2015) appear to have revealed several low-mass counterparts to the Octans-Near association.

In Section 6.5, four objects – A, I, K and X – pass tests for Octans-Near membership, however, target I is unlikely to be an Octans-Near member because the *UVW* error bars are so large that the fact it agrees with Octans-Near is not remarkable (see Section 7.1). Whether these objects are connected to either the Octans, the Octans-Near or not, there nevertheless still exists a sub-grouping of seven objects in the sample (A, B, D, F, K, X and Y) which are possibly coeval. All seven objects could be consistent with a common age of between 30 and 150 Myr, which is also consistent with Octans-Near. These have *UVW* values of $U = -10.5 \pm 2.7(\pm 1.8)$; $V = -4.3 \pm 1.0(\pm 1.4)$; $W = -4.9 \pm 3.6(\pm 1.3)\,\mathrm{km\,s^{-1}}$, which is close to Octans/Octans-Near but not to any other known MG (error bars are the standard deviations and the values in parentheses are the average *UVW* uncertainties). Of these seven, none are in similar in terms of *XYZ* positions, although five of them, A, B, D, F and Y, have sky positions within 3 h of right ascension of one another and 10 deg in declination. These are in the vicinity of the Pisces constellation, therefore if these did constitute an MG and were not associated with Octans-Near, we propose naming the ensemble as 'the Pisces moving group'.

In principle, if the seven kinematically consistent objects identified here were born from the same molecular cloud, then given their *UVWXYZ* coordinates, it would be possible to trace-back their motions under a reasonable gravitational potential and identify a time at which all these objects occupied a minimum. However, since our objects all have designated ages older than 30 Myr and lack trigonometric parallaxes, a kinematic traceback analysis is premature: it would only take 5 Myr for the current velocity uncertainties to produce a spatial dispersion equal to the current standard deviation of stellar positions.

8 CONCLUSIONS

From an initial sample of 146 spectroscopically observed, FGK stars with short rotation periods from the SuperWASP All Sky Survey, 26 were found to be Li-rich and therefore probably young by comparison with the photospheric Li abundance patterns seen in open clusters. Duplicate RV measurements suggest these are unlikely to be close binaries. Five objects were G-stars and the remaining 21 have spectral types from K0 to K6.

12 objects from the initial observed target sample had two or more RV measurements that varied by $>5\,\mathrm{km\,s^{-1}}$ on the time-scale of the observing run and are almost certain to be close, tidally-locked binary systems. This fraction of close binary systems is much higher than expected from a random sample of field stars, presumably because of our initial selection based on rapid rotation. If a significant Li line was not observed at the telescope, then usually a repeat measurement was not made. Of the remaining Li-depleted objects, for which only a single RV measurement was obtained, we anticipate that a large fraction will turn out to be close binary systems.

Typical ages of members in the likely-young sample are 30–200 Myr and have distances of 30–180 pc. Ages are primarily determined from lithium, but ages derived from rotation, activity and projected radius are usually in agreement, but might be compromised by binarity. Lower-mass, nearby, young stars are favourable as targets to follow-up with high-resolution imaging to detect the presence of brown-dwarf binaries, or even exoplanets. There are 16 objects in the likely-young sample with ages <200 Myr, later than K0 and within 100 pc that would be ideal candidates for imaging surveys.

54 per cent of the observed sample had rotation periods <2 d (77 out of 146) and there were 14 objects in the likely-young sample that had rotation periods less than 2 d. The sample may not be complete since sometimes even young stars do not exhibit significant rotational modulation. In terms of the distribution of rotation periods, the likely-young sample and parent sample have similar medians, therefore one would not gain by being more restrictive in choosing a rotation period cut-off.

11 targets are identified which satisfy kinematic and age criteria with at least one MG and 15 fail at least one criteria for membership of *any* of the MGs considered in this analysis. There is a low probability of the RVs being significantly in error due to binary motion (see Section 4.6), therefore it is unlikely that many of these classifications would change with more extensive RV observations. There is tentative evidence for a sub-grouping of seven objects that appear to be a Northern hemisphere counterpart to, but not identical to, the 'Octans-Near' MG proposed by Zuckerman et al. (2013). Regardless of whether some of these objects are connected to Octans-Near or not, a grouping of stars exist around $U = -10.5 \pm 2.7$; $V = -4.3 \pm 1.0$; $W = -4.9 \pm 3.6\,\mathrm{km\,s^{-1}}$ which we tentatively label as 'the Pisces moving group'.

In light of results from the analysis of these 146 objects, additional substantial surveys of MG candidates in the Northern hemisphere are desirable. The kinematically unbiased search mechanism was

~18 per cent efficient at detecting likely-single G and K-type stars younger than 200 Myr and can be used to identify stars that are not associated with previously studied MGs. More widespread searches for MG candidates in the Northern hemisphere may provide additional useful samples of young stars, and could unveil important kinematic substructure in the Solar neighbourhood.

ACKNOWLEDGEMENTS

We would like to thank the anonymous referee for a prompt review and for the comments which have greatly helped to improve the manuscript. Thanks are due to the staff at the NOT for their help during the observation. Particular thanks are owed to Eric Stempels for his use of the FIESTOOL package and Søren Frimann, who gave useful advice on using the data reduction pipeline. Thanks are also due to John Webb for constructing a comprehensive initial data search on the target stars, which served as a very useful reference. This research has made use of the SIMBAD data base, operated at CDS, Strasbourg, France. This publication makes use of data products from the Two Micron All Sky Survey, which is a joint project of the University of Massachusetts and the Infrared Processing and Analysis Center/California Institute of Technology, funded by the National Aeronautics and Space Administration and the National Science Foundation.

REFERENCES

Anders G. J., Coates D. W., Jeffries R. D., Kellett B. J., 1993, MNRAS, 265, 941
Barenfeld S. A., Bubar E. J., Mamajek E. E., Young P. A., 2013, ApJ, 766, 6
Barnes S. A., 2003, ApJ, 586, 464
Barnes S. A., 2007, ApJ, 669, 1167
Barrado y Navascués D., Deliyannis C. P., Stauffer J. R., 2001, ApJ, 549, 452
Biazzo K., Alcalá J. M., Covino E., Sterzik M. F., Guillout P., Chavarría-K. C., Frasca A., Raddi R., 2012, A&A, 542, A115
Binks A. S., Jeffries R. D., 2014, MNRAS, 438, L11
Boesgaard A. M., Tripicco M. J., 1986, ApJ, 303, 724
Bowler B. P., Liu M. C., Shkolnik E. L., Tamura M., 2015, ApJS, 216, 7
Brandt T. D. et al., 2014, ApJ, 786, 1
Canto Martins B. L., Lèbre A., Palacios A., de Laverny P., Richard O., Melo C. H. F., Do Nascimento J. D., Jr, de Medeiros J. R., 2011, A&A, 527, A94
Carlsson M., Rutten R. J., Bruls J. H. M. J., Shchukina N. G., 1994, A&A, 288, 860
Cayrel de Strobel G., Spite M., 1988, in Cayrel de Strobel G., Spite M., eds, Proc. IAU Symp. 132, The Impact of Very High S/N Spectroscopy on Stellar Physics. Kluwer, Dordrecht, p. 345
Chubak C., Marcy G., Fischer D. A., Howard A. W., Isaacson H., Johnson J. A., Wright J. T., 2012, preprint (arXiv:e-prints)
Collier Cameron A. et al., 2009, MNRAS, 400, 451
Cutri R. M. et al., 2003, 2MASS All Sky Catalog of Point Sources
da Silva L., Torres C. A. O., de La Reza R., Quast G. R., Melo C. H. F., Sterzik M. F., 2009, A&A, 508, 833
Dahm S. E., Simon T., 2005, AJ, 129, 829
de Bruijne J. H. J., Eilers A.-C., 2012, A&A, 546, A61
De Silva G. M., D'Orazi V., Melo C., Torres C. A. O., Gieles M., Quast G. R., Sterzik M., 2013, MNRAS, 431, 1005
Dent W. R. F. et al., 2013, PASP, 125, 477
Ducourant C., Teixeira R., Périé J. P., Lecampion J. F., Guibert J., Sartori M. J., 2005, A&A, 438, 769
Eggen O. J., 1961, R. Greenwich Obs. Bull., 41, 245
Eggen O. J., 1965, in Blaauw A., Schmidt M., eds, Galactic Structure. Univ. Chicago, Chicago, IL, p. 111
Eggen O. J., 1983, MNRAS, 204, 377
Epstein C. R., Pinsonneault M. H., 2014, ApJ, 780, 159
Fabricius C., Høg E., Makarov V. V., Mason B. D., Wycoff G. L., Urban S. E., 2002, A&A, 384, 180
Favata F., Barbera M., Micela G., Sciortino S., 1995, A&A, 295, 147
Fleming T. A., Molendi S., Maccacaro T., Wolter A., 1995, ApJS, 99, 701
Frasca A., Fröhlich H.-E., Bonanno A., Catanzaro G., Biazzo K., Molenda-Żakowicz J., 2011, A&A, 532, A81
Gagné J., Lafrenière D., Doyon R., Malo L., Artigau É., 2014, ApJ, 783, 121
Gagné J., Lafrenière D., Doyon R., Malo L., Artigau É., 2015, ApJ, 798, 73
Glebocki R., Gnacinski P., 2005, VizieR Online Data Catalog, 3244, 0
Güdel M., 2007, Living Rev. Sol. Phys., 4, 3
Hawley S. L., Reid I. N., Gizis J. E., Byrne P. B., 1999, in Butler C. J., Doyle J. G., eds, ASP Conf. Ser. Vol. 158, Solar and Stellar Activity: Similarities and Differences. Astron. Soc. Pac., San Francisco, p. 63
Henden A. A., Levine S. E., Terrell D., Smith T. C., Welch D., 2012, J. Am. Assoc. Var. Star Obs., 40, 430
Hogeveen S. J., 1990, Ap&SS, 173, 315
Hoogerwerf R., Blaauw A., 2000, A&A, 360, 391
Horne J. H., Baliunas S. L., 1986, ApJ, 302, 757
Innis J. L., Coates D. W., Thompson K., 1988, MNRAS, 233, 887
Isaacson H., Fischer D., 2010, ApJ, 725, 875
Jeffries R. D., 1995, MNRAS, 273, 559
Jeffries R. D., 2006, in Randich S., Pasquini L., eds, Pre-Main-Sequence Lithium Depletion. Springer-Verlag, Berlin, p. 163
Jeffries R. D., Jewell S. J., 1993, MNRAS, 264, 106
Jeffries R. D., Byrne P. B., Doyle J. G., Anders G. J., James D. J., Lanzafame A. C., 1994, MNRAS, 270, 153
Jeffries R. D., Totten E. J., James D. J., 2000, MNRAS, 316, 950
Jeffries R. D., Evans P. A., Pye J. P., Briggs K. R., 2006, MNRAS, 367, 781
Jeffries R. D. et al., 2014, A&A, 563, A94
Johnson D. R. H., Soderblom D. R., 1987, AJ, 93, 864
Jones D. H. P., 1971, MNRAS, 152, 231
Jones B. F., Shetrone M., Fischer D., Soderblom D. R., 1996, AJ, 112, 186
Jones B. F., Fischer D., Shetrone M., Soderblom D. R., 1997, AJ, 114, 352
Jones B. F., Fischer D., Soderblom D. R., 1999, AJ, 117, 330
King J. R., 1998, AJ, 116, 254
Kordopatis G. et al., 2013, AJ, 146, 134
Kraus A. L., Shkolnik E. L., Allers K. N., Liu M. C., 2014, AJ, 147, 146
Krishnamurthi A. et al., 1998, ApJ, 493, 914
Lagrange A.-M. et al., 2010, Science, 329, 57
Lépine S., Simon M., 2009, AJ, 137, 3632
Li J. Z., Hu J. Y., 1998, A&AS, 132, 173
Li J. Z., Hu J. Y., Chen W. P., 2000, A&A, 356, 157
Lomb N. R., 1976, Ap&SS, 39, 447
Luhman K. L., 2004, ApJ, 616, 1033
Makarov V. V., 2003, AJ, 126, 1996
Maldonado J., Martínez-Arnáiz R. M., Eiroa C., Montes D., Montesinos B., 2010, A&A, 521, A12
Malo L., Doyon R., Lafrenière D., Artigau É., Gagné J., Baron F., Riedel A., 2013, ApJ, 762, 88
Malo L., Artigau É., Doyon R., Lafrenière D., Albert L., Gagné J., 2014a, ApJ, 788, 81
Malo L., Doyon R., Feiden G. A., Albert L., Lafrenière D., Artigau É., Gagné J., Riedel A., 2014b, ApJ, 792, 37
Mamajek E. E., Hillenbrand L. A., 2008, ApJ, 687, 1264
Marois C., Macintosh B., Barman T., Zuckerman B., Song I., Patience J., Lafrenière D., Doyon R., 2008, Science, 322, 1348
Marois C., Zuckerman B., Konopacky Q. M., Macintosh B., Barman T., 2010, Nature, 468, 1080
Mason K. O. et al., 1995, MNRAS, 274, 1194
Maxted P. F. L. et al., 2011, PASP, 123, 547
Melis C., Reid M. J., Mioduszewski A. J., Stauffer J. R., Bower G. C., 2014, Science, 345, 1029
Meola G., Randich S., Pallavicini R., Stauffer J. R., Balachandran S., 2000, in Pallavicini R., Micela G., Sciortino S., eds, ASP Conf. Ser. Vol. 198,

Stellar Clusters and Associations: Convection, Rotation, and Dynamos. Astron. Soc. Pac., San Francisco, p. 285
Mermilliod J.-C., Mayor M., Udry S., 2009, A&A, 498, 949
Messina S., Desidera S., Turatto M., Lanzafame A. C., Guinan E. F., 2010, A&A, 520, A15
Mittag M., Hempelmann A., González-Pérez J. N., Schmitt J. H. M. M., Hall J. C., 2011, in Johns-Krull C., Browning M. K., West A. A., eds, ASP Conf. Ser. Vol. 448, 16th Cambridge Workshop on Cool Stars, Stellar Systems, and the Sun. Astron. Soc. Pac., San Francisco, p. 1187
Montes D., López-Santiago J., Fernández-Figueroa M. J., Gálvez M. C., 2001, A&A, 379, 976
Murphy S. J., Lawson W. A., Bessell M. S., 2013, MNRAS, 435, 1325
Murphy S. J., Lawson W. A., 2015, MNRAS, 447, 1267
Pace G., 2013, A&A, 551, L8
Panagi P. M., O'Dell M. A., 1997, A&AS, 121, 213
Patten B. M., Simon T., 1996, ApJS, 106, 489
Pecaut M. J., Mamajek E. E., 2013, ApJS, 208, 9
Perryman M. A. C. et al., 1998, A&A, 331, 81
Pinsonneault M. H., An D., Molenda-Żakowicz J., Chaplin W. J., Metcalfe T. S., Bruntt H., 2012, ApJS, 199, 30
Pollacco D. L. et al., 2006, PASP, 118, 1407
Raghavan D. et al., 2010, ApJS, 190, 1
Randich S., 2001, A&A, 377, 512
Randich S., Pallavicini R., Meola G., Stauffer J. R., Balachandran S. C., 2001, A&A, 372, 862
Reid N., Hawley S. L., Mateo M., 1995, MNRAS, 272, 828
Reinhold T., Reiners A., Basri G., 2013, A&A, 560, A4
Robin A. C., Marshall D. J., Schultheis M., Reylé C., 2012, A&A, 538, A106
Roeser S., Demleitner M., Schilbach E., 2010, AJ, 139, 2440
Santos N. C., Melo C., James D. J., Gameiro J. F., Bouvier J., Gomes J. I., 2008, A&A, 480, 889
Sarro L. M. et al., 2014, A&A, 563, A45
Scargle J. D., 1982, ApJ, 263, 835
Schlieder J. E., Lépine S., Simon M., 2010, AJ, 140, 119
Schlieder J. E., Lépine S., Simon M., 2012, AJ, 144, 109
Sestito P., Randich S., 2005, A&A, 442, 615
Shkolnik E. L., Liu M. C., Reid I. N., Dupuy T., Weinberger A. J., 2011, ApJ, 727, 6
Shkolnik E. L., Anglada-Escudé G., Liu M. C., Bowler B. P., Weinberger A. J., Boss A. P., Reid I. N., Tamura M., 2012, ApJ, 758, 56
Siess L., Dufour E., Forestini M., 2000, A&A, 358, 593
Soderblom D. R., 2010, ARA&A, 48, 581
Soderblom D. R., Oey M. S., Johnson D. R. H., Stone R. P. S., 1990, AJ, 99, 595
Soderblom D. R., Stauffer J. R., Hudon J. D., Jones B. F., 1993a, ApJS, 85, 315
Soderblom D. R., Pilachowski C. A., Fedele S. B., Jones B. F., 1993b, AJ, 105, 2299
Soderblom D. R., Jones B. F., Balachandran S., Stauffer J. R., Duncan D. K., Fedele S. B., Hudon J. D., 1993c, AJ, 106, 1059
Soderblom D. R., Fedele S. B., Jones B. F., Stauffer J. R., Prosser C. F., 1993d, AJ, 106, 1080
Soderblom D. R., Fedele S. B., Jones B. F., Stauffer J. R., Prosser C. F., 1995a, AJ, 109, 1402
Soderblom D. R., Jones B. F., Stauffer J. R., Chaboyer B., 1995b, AJ, 110, 729
Soderblom D. R., King J. R., Siess L., Jones B. F., Fischer D., 1999, AJ, 118, 1301
Spina L. et al., 2014, A&A, 567, A55
Stahler S. W., Palla F., 2005, The Formation of Stars. Wiley-VCH, New York
Stauffer J. R., Giampapa M. S., Herbst W., Vincent J. M., Hartmann L. W., Stern R. A., 1991, ApJ, 374, 142
Stauffer J. R., Hartmann L. W., Prosser C. F., Randich S., Balachandran S., Patten B. M., Simon T., Giampapa M., 1997, ApJ, 479, 776
Stauffer J. R., Schultz G., Kirkpatrick J. D., 1998, ApJ, 499, L199
Strassmeier K. G., Weber M., Granzer T., Järvinen S., 2012, Astron. Nachr., 333, 663
Tonry J., Davis M., 1979, AJ, 84, 1511
Torres C. A. O., da Silva L., Quast G. R., de la Reza R., Jilinski E., 2000, AJ, 120, 1410
Torres C. A. O., Quast G. R., da Silva L., de La Reza R., Melo C. H. F., Sterzik M., 2006, A&A, 460, 695
Torres C. A. O., Quast G. R., Melo C. H. F., Sterzik M. F., 2008, in Reipurth B., ed., Young Nearby Loose Associations, p. 757
Udry S., Mayor M., Queloz D., 1999, in Hearnshaw J. B., Scarfe C. D., eds, ASP Conf. Ser. Vol. 185, IAU Colloq. 170: Precise Stellar Radial Velocities. Astron. Soc. Pac., San Francisco, p. 367
van Leeuwen F., Alphenaar P., Brand J., 1986, A&AS, 65, 309
Viana Almeida P., Santos N. C., Melo C., Ammler-von Eiff M., Torres C. A. O., Quast G. R., Gameiro J. F., Sterzik M., 2009, A&A, 501, 965
Voges W. et al., 1999, A&A, 349, 389
Wilden B. S., Jones B. F., Lin D. N. C., Soderblom D. R., 2002, AJ, 124, 2799
Worley C. E., Douglass G. G., 1997, A&AS, 125, 523
Xing L.-F., Xing Q.-F., 2012, A&A, 537, A91
Zacharias N., Monet D. G., Levine S. E., Urban S. E., Gaume R., Wycoff G. L., 2005, VizieR Online Data Catalog, 1297, 0
Zechmeister M., Kürster M., 2009, A&A, 496, 577
Zuckerman B., Song I., 2004, ARA&A, 42, 685
Zuckerman B., Webb R. A., 2000, ApJ, 535, 959
Zuckerman B., Song I., Bessell M. S., Webb R. A., 2001, ApJ, 562, L87
Zuckerman B., Vican L., Song I., Schneider A., 2013, ApJ, 778, 5

SUPPORTING INFORMATION

Additional Supporting Information may be found in the online version of this paper:

lightcurves.pdf (http://mnras.oxfordjournals.org/lookup/suppl/doi:10.1093/mnras/stv1309/-/DC1).

Please note: Oxford University Press is not responsible for the content or functionality of any supporting materials supplied by the authors. Any queries (other than missing material) should be directed to the corresponding author for the paper.

This paper has been typeset from a TEX/LATEX file prepared by the author.